

Electron Heat Flux in the Solar Wind: Generalized Approaches to Fluid Transport with a Variety of Skewed Velocity Distributions

Steven R. Cranmer¹ and Avery J. Schiff^{1,2}

¹Department of Astrophysical and Planetary Sciences, Laboratory for Atmospheric and Space Physics,
University of Colorado, Boulder, CO 80309, USA

²Myriad Genetics, Salt Lake City, UT 84108, USA

Key Points:

- Understanding coronal heating and solar wind acceleration requires an accurate description of heat conduction beyond Spitzer-Härm theory.
- Fluid-moment models of parallel electron heat conduction are constructed using skewed, positive-definite velocity distributions.
- Both analytic models and fits to in situ data can be used to constrain parameters of closed-form solutions for the collisionless heat flux.

arXiv:2109.15267v1 [astro-ph.SR] 30 Sep 2021

Abstract

In the solar corona and solar wind, electron heat conduction is an important process that transports energy over large distances and helps determine the spatial variation of temperature. High-density regions undergoing rapid particle-particle collisions exhibit a heat flux described well by classical Spitzer-Härm theory. However, much of the heliosphere is closer to a more collisionless state, and there is no standard description of heat conduction for fluid-based (e.g., magnetohydrodynamic) models that applies generally. Some proposed models rely on electron velocity distributions that exhibit negative values of the phase-space density. In this paper, we explore how positive-definite velocity distributions can be used in fluid-based conservation equations for the electron heat flux along magnetic-field lines in the corona and solar wind. We study both analytic forms of skewed distributions (e.g., skew-normal distributions, two-sided bi-Maxwellians, and constant-collision-time electrostatic solutions) and empirical fits to measurements of core, halo, and strahl electrons in interplanetary space. We also present example solutions to a generalized conservation equation for the heat flux in the solar wind, with some limiting cases found to resemble known free-streaming approximations. The resulting values of the electron heat flux vary as a function of radial distance and Knudsen number in ways that resemble observed data. We note that this model does not include the effects of kinetic instabilities (which may impose saturation limits when active), so for now its regime of applicability is limited to collisionless heat-flux evolution away from the known instability boundaries in parameter space.

Plain Language Summary

The solar corona is a layer of hot (million-degree Celsius) gas that surrounds the Sun and expands into interplanetary space as the rapidly accelerating solar wind. Because the gas is so hot, its atoms become ionized on their journey from the solar surface. The nuclei of the former atoms are the heaviest of the new particles, so they carry most of the solar wind’s mass. However, most of its heat is carried by the rapidly-moving electrons that once orbited those nuclei. When close to the Sun, electrons transport heat in much the same way as they do in metal objects on Earth: random collisions cause the heat to conduct from hot to cold regions. We study their behavior higher above the Sun’s surface, where the density of particles plummets and random collisions become infrequent. In these essentially collision-free regions, electrons still carry heat, but they do it because the solar wind’s expansion causes them to develop unusually shaped probability distributions of velocity. We explore various mathematical forms for those distributions and show how they can be used to accurately determine the strength of heat conduction in future computer simulations of the corona and solar wind.

1 Introduction

The Sun’s combined corona/heliosphere system is a hot (i.e., nearly fully ionized) and expanding plasma composed of mostly hydrogen, some helium, and a small fraction of heavier elements. Despite the negligibly small masses of the free electrons in such a plasma, these particles are important to maintaining overall quasi-neutrality and a zero-current electrostatic balance. In situ measurements have revealed that the electron velocity distribution function (VDF) often shows four relatively distinct components: (1) an approximately Maxwellian *core*, often close to being in thermal equilibrium with the protons, (2) a higher-energy isotropic *halo*, usually with a mild power-law tail in velocity space, (3) a magnetic-field-aligned beam or *strahl* that indicates connectivity to the near-Sun corona, and (4) a much higher-energy isotropic power-law *super-halo* (Pilipp et al., 1987; Lin et al., 1997; Wang et al., 2015). Interactions between these components give rise to macroscopic phenomena such as heat conduction, and they determine the

state of several key kinetic instabilities (see, e.g., Feldman et al., 1975; Marsch, 2006; Verscharen et al., 2019).

Particle-particle collisions are infrequent in a plasma as rarefied as the solar wind. There have been many useful insights gained from a fully kinetic “exospheric” approach to modeling these kinds of systems (e.g., Lemaire & Scherer, 1973; Meyer-Vernet, 1999; Zouganelis et al., 2004; Echim et al., 2011). It has generally been presumed to be unwise to model collisionless plasmas as fluids; i.e., to use moment-based equations of hydrodynamics or magnetohydrodynamics (MHD). In addition to assuming frequent collisions, many of these sets of conservation equations are based on the assumption of perfectly Maxwellian VDFs. Nevertheless, fluid-based modeling has been quite successful in predicting many large-scale properties of the corona and solar wind (Parker, 1958; Withbroe, 1988; Linker et al., 1999; Gombosi et al., 2018). Also, the existence of quasi-Maxwellian cores in the electron, proton, and heavy-ion VDFs—often observed in regions of space where the collisionless theory predicts they should not exist—points to some kind of velocity-space randomization that plays a similar thermalizing role as particle collisions.

In order to expand the usefulness of fluid-based modeling to regimes of lower collisionality, it is necessary to build in compatibility with non-Maxwellian particle distributions. Some attempts to do this have relied on polynomial-type perturbations to an underlying Maxwellian (e.g., Schunk, 1977; Cuperman & Dryer, 1985; Olsen & Leer, 1996) that have the side-effect of making the VDF unphysically negative in some regions of velocity space. Thus, in this paper, we begin to explore other ways to use moment-based conservation equations that are compatible with positive-definite non-Maxwellian VDFs. For now, we focus on one specific physical process: skewness in the electron distribution function that gives rise to a nonzero heat flux. We derive a generalized third-moment conservation equation that reproduces classical Spitzer & Härm (1953) thermal conductivity in the limit of rapid collisions, but also can be applied to more collisionless free-streaming regimes of the solar wind.

Section 2 of this paper defines several key properties of the electron VDF—including shape-dependent coefficients related to the partitioning of energy in third-order and fourth-order moments—and describes generalized conservation equations for the moments. Section 3 examines a series of different formulations for the shapes of skewed VDFs that carry nonzero heat flux along magnetic-field lines. Section 4 presents example calculations for the heat flux, compares with observational data, and shows how some traditional analytic limits (e.g., Hollweg, 1974, 1976) can be considered as special cases of the theory developed in this paper. Section 5 summarizes the major results of this paper and discusses some broader implications.

2 Generalized Conservation Equations

In order to devise new ways of modeling the electron heat flux, we first must describe the shape of the VDF and the behavior of its kinetic moments as a function of space and time. Section 2.1 sets up the required definitions, and Section 2.2 shows how the fluid-moment conservation equations reduce to simpler forms when studying time-steady electron transport along magnetic-field lines. Section 2.3 ties down the terms in these equations that describe Coulomb collisions and shows how classical Spitzer & Härm (1953) conductivity can be made to apply when those collisions are rapid.

2.1 Moments in Velocity Space

The primary quantities to be modeled are the electron phase-space VDF $f(\mathbf{v})$ and its velocity-space moments. Our notation mainly follows Schunk (1977), but there are a number of other useful and definitive derivations of these quantities (e.g., Braginskii, 1965; Chapman & Cowling, 1970; Barakat & Schunk, 1982; Struchtrup, 2005; Chust &

Belmont, 2006; Hunana et al., 2019a, 2019b). The number density is the zeroth moment (i.e., just the integral over all velocity space) of the VDF,

$$n = \int d^3\mathbf{v} f(\mathbf{v}) . \quad (1)$$

Higher moments are described by weighted averages of the form

$$\langle \Phi(\mathbf{v}) \rangle = \frac{\int d^3\mathbf{v} f(\mathbf{v}) \Phi(\mathbf{v})}{\int d^3\mathbf{v} f(\mathbf{v})} \quad (2)$$

where $\Phi(\mathbf{v})$ can be a scalar, vector, or tensor function of the scalar components of \mathbf{v} . The first moment, the bulk fluid velocity, is defined as $\mathbf{u} = \langle \mathbf{v} \rangle$. Most higher moments make use of the velocity measured in the bulk-flow frame, $\mathbf{c} = \mathbf{v} - \mathbf{u}$, which is sometimes called the peculiar or random velocity.

We define the second-rank (3×3) pressure tensor and third-rank ($3 \times 3 \times 3$) heat-flow tensor, using dyadic notation, as

$$\mathcal{P} = nm\langle \mathbf{c}\mathbf{c} \rangle , \quad \mathcal{Q} = nm\langle \mathbf{c}\mathbf{c}\mathbf{c} \rangle , \quad (3)$$

where m refers to the electron mass. Later we often make use of various contracted forms of these tensors, such as the scalar pressure

$$p = \frac{1}{3} \text{Tr}(\mathcal{P}) = \frac{1}{3} \sum_{i=1}^3 \mathcal{P}_{ii} \quad (4)$$

and the heat-flux vector

$$\mathbf{q} = \frac{1}{2} nm \langle c^2 \mathbf{c} \rangle . \quad (5)$$

Lastly, we define a fourth-order thermodynamic quantity, for which only a second-rank tensor contraction is needed,

$$\mathcal{R} = \frac{1}{2} nm \langle c^2 \mathbf{c}\mathbf{c} \rangle , \quad (6)$$

and the divergence of this quantity is included in the conservation equation for heat flux.

Conservation equations for the VDF moments are constructed by taking appropriate moments of the Boltzmann transport equation. Because we primarily want to study the effects of VDF skewness on the evolution of the heat flux \mathbf{q} , we make several simplifications to isolate these effects from those introduced by other processes:

1. Although the general problem of deriving a set of fluid-moment closure equations usually involves the need to include a range of source/sink terms (e.g., external forces in the momentum equation or explicit heating/cooling terms in the thermal energy equation), we will not include them here. See, however, Section 4.3 for some additional discussion of these effects.
2. For now, we will use only the collisionless Vlasov form of the Boltzmann equation. The effects of electron–electron Coulomb collisions (e.g., Braginskii, 1965) will be reincorporated in an approximate way later.
3. In the absence of VDF skewness, we generally assume the distribution function is isotropic, such that the pressure tensor is diagonal and given by $p\mathcal{I}$ (where \mathcal{I} is the 3×3 identity matrix). This sets all stress-tensor terms to zero and eliminates viscosity from the system.

Thus, we follow equation (20) of Schunk (1977) and write the momentum conservation equation as

$$nm \frac{D\mathbf{u}}{Dt} + \nabla p = 0 , \quad (7)$$

where the advective derivative D/Dt is defined as $\partial/\partial t + \mathbf{u} \cdot \nabla$. The thermal energy conservation equation is given by

$$\frac{3}{2} \frac{Dp}{Dt} + \frac{3}{2} p (\nabla \cdot \mathbf{u}) + \mathcal{P} : \nabla \mathbf{u} + \nabla \cdot \mathbf{q} = 0 \quad (8)$$

where the colon denotes a tensor double dot product. Finally, the heat-flux conservation equation is

$$\frac{D\mathbf{q}}{Dt} + \mathbf{q} \cdot \nabla \mathbf{u} + \mathbf{q} (\nabla \cdot \mathbf{u}) + \mathcal{Q} : \nabla \mathbf{u} + \nabla \cdot \mathcal{R} + \left[\frac{D\mathbf{u}}{Dt} \cdot \left(\frac{5}{2} p \mathcal{I} \right) \right] = 0. \quad (9)$$

Given the assumptions listed above, these equations are exact and do not involve any artificial closure truncations.

2.2 Transport along Magnetic Flux Tubes

Many of the vector and tensor terms in the fluid conservation equations are simplified substantially when restricting the geometry to one-dimensional trajectories parallel to a large-scale magnetic field. Anticipating application to the global corona and heliosphere, we set up a spherical coordinate system in which the magnetic field is pointed radially away from the origin along the polar axis, and the only direction along which quantities can vary is r . Thus, all partial derivatives with respect to the locally transverse coordinates (θ and ϕ) are zero. However, we include the effect of *flux-tube expansion*; i.e., the nonradial spreading of slightly off-axis field lines centered around the polar axis. The properties of field-line coordinate systems like this have been studied extensively (see, e.g., Zawaideh et al., 1988; Gombosi & Rasmussen, 1991; Wu & Taieb, 1993; Li & Li, 2006).

If the magnitude of the magnetic field varies along the polar axis as $B(r)$, then the cross-sectional area of an idealized flux tube is given by the conservation of magnetic flux as $A(r) \propto 1/B(r)$. This means that vector gradients and divergences can be written as

$$\nabla f = \frac{\partial f}{\partial r} \hat{\mathbf{e}}_r, \quad \nabla \cdot \mathbf{F} = \frac{1}{A} \frac{\partial}{\partial r} (A F_r), \quad (10)$$

where $\hat{\mathbf{e}}_r$ is the radial unit vector. Let us also assume that the only nonzero component of the solar-wind bulk velocity \mathbf{u} is its radial (i.e., field-aligned) component u_r , so that, for example,

$$\mathcal{P} : \nabla \mathbf{u} = \mathcal{P}_{rr} \frac{\partial u_r}{\partial r} + (\mathcal{P}_{\theta\theta} + \mathcal{P}_{\phi\phi}) \frac{u_r}{2A} \frac{\partial A}{\partial r}. \quad (11)$$

Note that the adopted coordinates do not account for the Parker spiral effect in the heliosphere; i.e., the misalignment of the radial bulk flow and magnetic field directions in the ecliptic plane. See, for example, Li (1999) for extensions to the conservation equations that take this effect into account.

Making use of additional identities for the flux-tube geometry, the thermal energy equation can be written in these coordinates as

$$\frac{3}{2} \frac{\partial p}{\partial t} + \frac{3}{2} u_r \frac{\partial p}{\partial r} + \frac{5}{2} \frac{p}{A} \frac{\partial}{\partial r} (u_r A) + \frac{1}{A} \frac{\partial}{\partial r} (q_r A) = 0. \quad (12)$$

Also, combining the radial components of equations (7) and (9) gives the field-aligned component of the heat-flux equation:

$$\begin{aligned} \frac{\partial q_r}{\partial t} + u_r \frac{\partial q_r}{\partial r} + q_r \frac{\partial u_r}{\partial r} + \frac{q_r}{A} \frac{\partial}{\partial r} (u_r A) + \mathcal{Q}_{rrr} \frac{\partial u_r}{\partial r} + (\mathcal{Q}_{r\theta\theta} + \mathcal{Q}_{r\phi\phi}) \frac{u_r}{2A} \frac{\partial A}{\partial r} + \\ + \frac{1}{A} \frac{\partial}{\partial r} (\mathcal{R}_{rr} A) - (\mathcal{R}_{\theta\theta} + \mathcal{R}_{\phi\phi}) \frac{1}{2A} \frac{\partial A}{\partial r} - \frac{5p}{2nm} \frac{\partial p}{\partial r} = 0. \end{aligned} \quad (13)$$

We can simplify the third-order quantities above by using the moment definitions to show that

$$q_r = \frac{1}{2} (\mathcal{Q}_{rrr} + \mathcal{Q}_{r\theta\theta} + \mathcal{Q}_{r\phi\phi}) . \quad (14)$$

For the gyrotropic VDFs considered in this paper, we can also note that $\mathcal{Q}_{r\theta\theta} = \mathcal{Q}_{r\phi\phi}$. We found that it is useful to write equation (14) using dimensionless partition fractions α_{\parallel} and α_{\perp} , such that

$$\mathcal{Q}_{rrr} = 2\alpha_{\parallel}q_r , \quad \mathcal{Q}_{r\theta\theta} = \mathcal{Q}_{r\phi\phi} = \alpha_{\perp}q_r \quad (15)$$

and

$$\alpha_{\parallel} + \alpha_{\perp} = 1 . \quad (16)$$

Also, we define

$$\mathcal{R}_{rr} = \eta_{\parallel} \frac{5p^2}{2mn} , \quad \mathcal{R}_{\theta\theta} = \mathcal{R}_{\phi\phi} = \eta_{\perp} \frac{5p^2}{2mn} \quad (17)$$

and we anticipate the results of Section 3 to note that, in many cases, $\eta_{\parallel} \approx \eta_{\perp} \approx 1$.

We use notation defined above, together with the addition of a schematic collision term on the right-hand side, to rewrite the heat-flux conservation equation as

$$\begin{aligned} & \frac{\partial q_r}{\partial t} + u_r \frac{\partial q_r}{\partial r} + (1 + \alpha_{\parallel}) 2q_r \frac{\partial u_r}{\partial r} + (1 + \alpha_{\perp}) \frac{q_r u_r}{L_A} + \\ & + \frac{5}{2} (\eta_{\parallel} - \eta_{\perp}) \frac{p^2}{mnL_A} + \frac{5}{2} (\eta_{\parallel} - 1) \frac{p}{mn} \frac{\partial p}{\partial r} + \frac{5p\eta_{\parallel}}{2m} \frac{\partial}{\partial r} \left(\frac{p}{n} \right) = -\nu_{\text{eff}} q_r , \end{aligned} \quad (18)$$

where we simplify a few of the terms by defining a flux-tube expansion scale length

$$L_A = \frac{A}{\partial A / \partial r} . \quad (19)$$

Equation (18) introduces an effective electron–electron collision frequency ν_{eff} , and we derive a more detailed expression for it in Section 2.3.

There are several ways of solving the above equations for the electron heat flux. In the limit of a steady-state system (i.e., in which all time derivatives are zero), equation (18) is an ordinary differential equation for $q_r(r)$. Schiff (2020) explored numerical solutions to this equation when the other moments (n , u_r , p) are specified independently and the VDF-dependent coefficients (α_{\parallel} , α_{\perp} , η_{\parallel} , η_{\perp}) are given by the Grad-model values discussed in Section 3.2 below. Here, we follow Cuperman & Dryer (1985), who showed how equation (12) can be solved for $\partial q_r / \partial r$ and substituted into equation (18) to provide a direct analytic solution for q_r . Using the notation developed above, we express this solution as

$$q_r = \frac{q_{\text{num}}}{q_{\text{den}}} , \quad (20)$$

with

$$q_{\text{num}} = \frac{3u_r^2}{5} \frac{\partial p}{\partial r} + \frac{u_r^2 p}{L_A} + u_r p \frac{\partial u_r}{\partial r} + \frac{(\eta_{\perp} - \eta_{\parallel}) p^2}{mnL_A} + (1 - \eta_{\parallel}) \frac{p}{mn} \frac{\partial p}{\partial r} - \eta_{\parallel} \frac{p}{m} \frac{\partial}{\partial r} \left(\frac{p}{n} \right) \quad (21)$$

$$q_{\text{den}} = \frac{4}{5} (1 + \alpha_{\parallel}) \frac{\partial u_r}{\partial r} + \frac{2\alpha_{\perp} u_r}{5L_A} + \frac{2}{5} \nu_{\text{eff}} . \quad (22)$$

Once we compute representative values for some of the higher-moment constants (e.g., α_{\parallel} , α_{\perp} , η_{\parallel} , η_{\perp}) in Section 3, we present a range of example solutions for q_r in Section 4.

2.3 Incorporating Coulomb Collisions

The magnitude of the effective collision rate ν_{eff} can be estimated by referring to the classical (Spitzer & Härm, 1953; Braginskii, 1965) results for a strongly collisional and fully ionized plasma. That case is written as

$$q_r = -\frac{\kappa_0 T^{5/2}}{\ln \Lambda} \frac{\partial T}{\partial r}, \quad (23)$$

where $\kappa_0 = 1.84 \times 10^{-10} \text{ W m}^{-1} \text{ K}^{-7/2}$ and $\ln \Lambda$ is the Coulomb logarithm. We also assume the isotropic ideal-gas law $p = nk_{\text{B}}T$, where k_{B} is Boltzmann’s constant. The above expression can be shown to be equivalent to equations (20)–(22) in the limit of strong collisions, no outflow ($u_r = 0$), and relatively weak skewness ($\eta_{\parallel} = \eta_{\perp} = 1$). In that case, only the final terms in each of equations (21) and (22) survive, and the heat flux is given by

$$q_r \approx -\frac{5p}{2m\nu_{\text{eff}}} \frac{\partial}{\partial r} \left(\frac{p}{n} \right) = -\frac{5nk_{\text{B}}^2 T}{2m\nu_{\text{eff}}} \frac{\partial T}{\partial r}, \quad (24)$$

and we emphasize the assumption of $\eta_{\parallel} = 1$ here. A generic electron–electron collision rate can be written as

$$\nu_{\text{eff}} = \frac{\xi e^4 n \ln \Lambda}{16\pi\epsilon_0^2 m_e^{1/2} (k_{\text{B}}T)^{3/2}}, \quad (25)$$

where e is the electron charge, ϵ_0 is the vacuum electric permittivity, and ξ is a dimensionless factor. For specific models of the skewed VDF, such as those discussed below in Section 3, it is possible to evaluate the Boltzmann collision term to determine self-consistent expressions for ξ (see, for example, Killie et al., 2004). However, in this paper we take a shortcut that presumes the Spitzer & Härm (1953) result is always valid in the limit of rapid collisions, and thus we aim to determine the value of ξ required to make that happen. Thus, incorporating equation (25) into equation (24) and comparing with equation (23), we notice the following identity,

$$\kappa_0 = \frac{40\pi\epsilon_0^2 k_{\text{B}}^{7/2}}{\xi m_e^{1/2} e^4} = \frac{1.5318 \times 10^{-10} \text{ W m}^{-1} \text{ K}^{-7/2}}{\xi}, \quad (26)$$

and a specific value of $\xi = 0.8325$ would be required to ensure equality with the Spitzer & Härm (1953) conductivity. Additional complications that arise for $\eta_{\parallel} \neq 1$ are discussed in Section 4.1 below.

3 Skewed Velocity Distribution Functions

The goal of this paper is to show how equations (20)–(22) can be used to compute values of the electron heat flux that apply in regions bridging the collisional and collisionless regimes. To do that, values for the higher-moment VDF parameters (e.g., α_{\parallel} , α_{\perp} , η_{\parallel} , η_{\perp}) must be known. Here, we evaluate those parameters for a range of different analytic expressions of skewed VDFs. These distributions are all assumed to be gyrotropic; i.e., they are symmetric along all velocity-space axes transverse to the magnetic field, and they depend explicitly only on velocity components $v_{\parallel} = v_r$ and $v_{\perp} = (v_{\theta}^2 + v_{\phi}^2)^{1/2}$.

3.1 Classical Non-Skewed Basis Functions

Because we generally treat skewness as a perturbation to an underlying equilibrium distribution, the properties of those non-skewed VDFs should first be specified. Note, however, that other approaches have been adopted. For example, Morse & Nielson (1973) learned a lot about the physics of heat flux by using simple piecewise-constant VDFs. However, for applications to the solar wind, we find that the Maxwell-Boltzmann distribution— together with two of its most common non-skewed generalizations—is a preferable foundation to build upon.

The first generalization is the bi-Maxwellian VDF:

$$f(\mathbf{v}) = \frac{n}{\pi^{3/2} w_{\parallel} w_{\perp}^2} \exp \left[-\frac{(v_{\parallel} - u_{\parallel})^2}{w_{\parallel}^2} - \frac{v_{\perp}^2}{w_{\perp}^2} \right], \quad (27)$$

where the thermal speeds are defined as $w_{\parallel}^2 = 2k_{\text{B}}T_{\parallel}/m$ and $w_{\perp}^2 = 2k_{\text{B}}T_{\perp}/m$. The distribution is normalized such that both n and u_{\parallel} are the results for the zeroth and first moments. In general, the pressure tensor is not isotropic, since

$$\mathcal{P}_{rr} = \frac{1}{2} m n w_{\parallel}^2, \quad \mathcal{P}_{\theta\theta} = \mathcal{P}_{\phi\phi} = \frac{1}{2} m n w_{\perp}^2, \quad (28)$$

and the isotropic Maxwellian distribution is given when $w_{\parallel} = w_{\perp} \equiv w$. In that limiting case,

$$p = n k_{\text{B}} \left(\frac{T_{\parallel} + 2T_{\perp}}{3} \right) = n k_{\text{B}} T = \frac{1}{2} n m w^2. \quad (29)$$

Because equation (27) has no skewness, the corresponding heat flux vector \mathbf{q} is identically zero and the α_{\parallel} and α_{\perp} coefficients are undefined. However, we can use the second-order moments to define a saturated heat flux q_0 , i.e., the flux corresponding to a plasma that transports its own thermal energy density at the local thermal speed. One traditional definition for this quantity is

$$q_0 = \frac{3}{2} n k_{\text{B}} T \sqrt{\frac{2k_{\text{B}}T}{m}} \quad (30)$$

though other versions—essentially the above expression multiplied by other order-unity constants—have been proposed (see, e.g., Parker, 1964; Cowie & McKee, 1977; Smith & Lillequist, 1979). For a bi-Maxwellian distribution we assume the transport is taking place along the r direction (i.e., parallel to the field), so that

$$q_0 = \frac{m n w_{\parallel}}{2} \left(\frac{w_{\parallel}^2}{2} + w_{\perp}^2 \right). \quad (31)$$

Also, the fourth-order moments are specified by

$$\mathcal{R}_{rr} = m n \left(\frac{3}{8} w_{\parallel}^4 + \frac{1}{4} w_{\parallel}^2 w_{\perp}^2 \right), \quad \mathcal{R}_{\theta\theta} = \mathcal{R}_{\phi\phi} = m n \left(\frac{1}{8} w_{\parallel}^2 w_{\perp}^2 + \frac{1}{2} w_{\perp}^4 \right). \quad (32)$$

In the isotropic limit, these expressions combine with equation (17) to provide

$$\eta_{\parallel} = \eta_{\perp} = 1. \quad (33)$$

Another way to generalize the Maxwellian distribution is to add a suprathermal power-law tail. In space physics, a common way to parameterize this kind of VDF is the kappa (Olbert, 1968; Vasyliunas, 1968; Livadiotis & McComas, 2013) or bi-kappa (e.g., Summers & Thorne, 1992) distribution. Here, we discuss only the isotropic kappa distribution, for which the primary independent variable is the magnitude of the peculiar velocity $c = |\mathbf{v} - \mathbf{u}|$, with

$$f(\mathbf{v}) = \frac{n \Gamma(\kappa + 1)}{\pi^{3/2} w^3 (\kappa - 3/2)^{3/2} \Gamma(\kappa - 1/2)} \left[1 + \frac{c^2}{w^2 (\kappa - 3/2)} \right]^{-1-\kappa}. \quad (34)$$

This expression reduces to a Maxwellian distribution in the limit $\kappa \rightarrow \infty$. With the form of f given above, the second moment converges to the usual value ($p = n k_{\text{B}} T$) only for $\kappa > 3/2$ and diverges for smaller values of κ . Keeping the fourth moment finite provides a more stringent limit on the κ exponent, with

$$\eta_{\parallel} = \eta_{\perp} = \frac{\kappa - 3/2}{\kappa - 5/2} \quad (35)$$

only being valid for $\kappa > 5/2$. Note that the existence of suprathermal power-law wings enhances these quantities over their equivalent Maxwellian values. For typical values of κ of order 3 to 5, the above values of η_{\parallel} and η_{\perp} can range between 1.4 and 3.

3.2 Grad-Type Polynomial Expansions

There are several long-studied ways of perturbing a zeroth-order non-skewed VDF to be able to solve for transport coefficients such as the heat flux. The Chapman–Enskog approach (see, e.g., Chapman & Cowling, 1970) involves expanding the distribution function in powers of the Knudsen number (see Section 4.2) and truncating the expansion to be consistent with a finite number of moment-based fluid equations. In the Grad (1949) approach, perturbations to the VDF are expressed as Hermite polynomials, with coefficients determined by demanding consistency with a finite number of moments. Here, we focus on Grad-type expansions investigated by Schunk (1977) and Killie et al. (2004), but note that other related alternatives exist (see, e.g., Whang, 1971; Chiuderi et al., 2011). We must also mention that these expansion-based VDFs all tend to exhibit a clearly undesirable feature: they require that some regions of velocity space have $f(\mathbf{v}) < 0$. This unphysical property is discussed further below.

Schunk (1977) developed the classical Grad (1949) expansion, also known as the eight-moment approximation, whose VDF can be written as

$$f(\mathbf{v}) = \frac{n}{\pi^{3/2}w^3} \exp\left(-\frac{c^2}{w^2}\right) \left[1 - \frac{3q_r c_{\parallel}}{q_0 w} \left(1 - \frac{2c^2}{5w^2}\right)\right]. \quad (36)$$

Note that Demars & Schunk (1979) generalized this to an even more general expansion around a bi-Maxwellian basis function. In equation (36), the saturated heat flux is given by its isotropic Maxwellian limit, $q_0 = (3/4)mnw^3$. This distribution has been parameterized so that the zeroth, first, second, and third moments all work out to their proper values as defined above, no matter how large is the specified value of q_r/q_0 . The components of the heat-flux tensor correspond to values of

$$\alpha_{\parallel} = \frac{3}{5}, \quad \alpha_{\perp} = \frac{2}{5}. \quad (37)$$

Also, this VDF shares the same fourth-order moment behavior as the corresponding Maxwellian (i.e., the limit $q_r \rightarrow 0$) in that the \mathcal{R} tensor is diagonal, with $\eta_{\parallel} = \eta_{\perp} = 1$.

Killie et al. (2004) noted that the first-order corrections to a Maxwellian in equation (36) do not agree with the expected velocity-space scalings of Spitzer & Härm (1953) theory, so they proposed a revised version:

$$f(\mathbf{v}) = \frac{n}{\pi^{3/2}w^3} \exp\left(-\frac{c^2}{w^2}\right) \left[1 - \frac{6q_r c_{\parallel} c^2}{5q_0 w^3} \left(1 - \frac{2c^2}{7w^2}\right)\right]. \quad (38)$$

Despite the fact that equation (38) results in a significant improvement in accuracy for the Coulomb collision term, in comparison with equation (36), all of the moments defined in this paper are identical for the Killie et al. (2004) and Schunk (1977) forms of the VDF.

Figure 1a shows an example VDF, using the Schunk (1977) form, as contours in gyrotropic (v_{\parallel}, v_{\perp}) coordinates. Note the existence of multiple regions of velocity space in which $f < 0$. One way of thinking about these regions is that the conservation of system-wide quantities like mass, momentum, and energy comes at the expense of creating a small population of unphysical “antiparticles.” Scudder (2019, 2021) discussed several reasons why these kinds of VDFs should not be used, especially when the magnitudes of the skewness and heat flux become large. Thus, we include a discussion of these distributions mainly for completeness, and we do not recommend basing solutions to equations (20)–(22) on their properties.

3.3 Two-Sided Bi-Maxwellians

The remaining four subsections of Section 3 involve finding ways of representing skewness in an electron VDF without creating regions of negative $f(\mathbf{v})$.

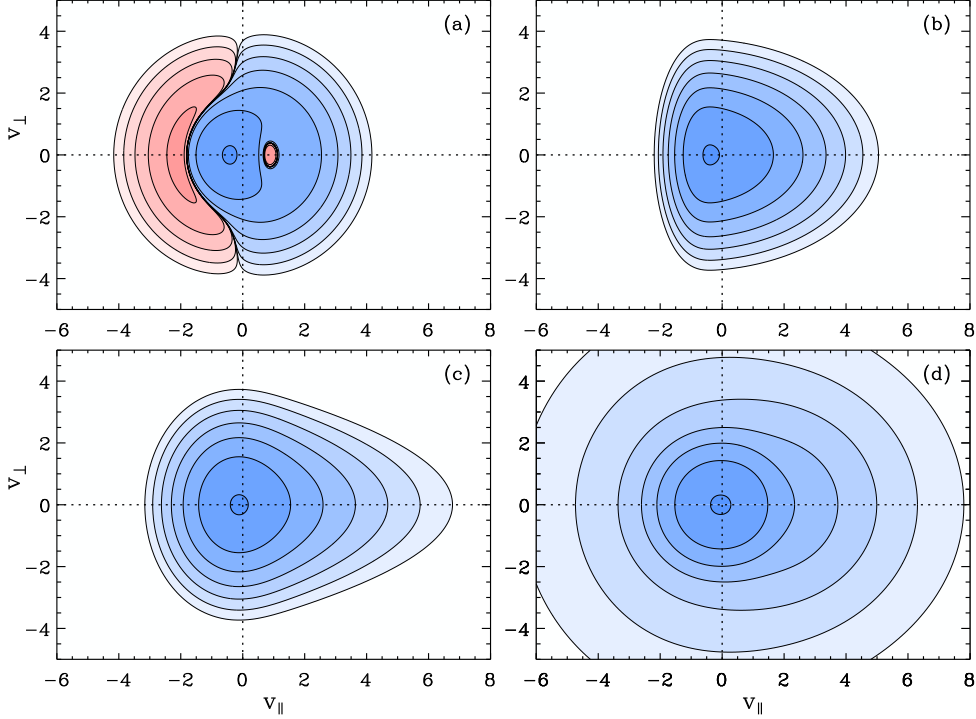


Figure 1. Example skewed VDFs, plotted as one-per-decade contours with $f > 0$ (blue) and $f < 0$ (red), each starting at ± 0.9 times the peak value in each case. Velocities v_{\parallel} and v_{\perp} are given in units of each distribution’s thermal speed w , and have been shifted to put the bulk speed \mathbf{u} at the origin. (a) Schunk (1977) VDF with $q_r/q_0 = 0.6$. (b) Skew-normal VDF with $\sigma_s = 3.9$. (c) Whealton & Woo (1972) VDF with $\sigma_w = 1.4$. (d) *Wind* VDF fit from 16 April 1999, 10:30:27 UT (Wilson et al., 2019a).

One straightforward way to specify a skewed VDF would be to assign different thermal widths to the two halves of the distribution corresponding to particles moving in the $+r$ and $-r$ directions. Something similar to this idea has been used, for kappa distributions, by Lazar et al. (2012). Also, studies of rarefied gas flows in the vicinity of a solid, flat plane traditionally use a similar kind of two-sided distribution (e.g., El-Sakka et al., 1985). The basic form of the proposed VDF, written in a frame at rest for an unskewed distribution, is

$$f(\mathbf{v}) = \frac{2n}{\pi^{3/2}w_0^2(w_1 + w_2)} \exp\left(-\frac{v_{\perp}^2}{w_0^2}\right) \times \begin{cases} \exp(-v_{\parallel}^2/w_1^2) & \text{for } v_{\parallel} < 0, \\ \exp(-v_{\parallel}^2/w_2^2) & \text{for } v_{\parallel} \geq 0 \end{cases} \quad (39)$$

where the three thermal speeds (w_0, w_1, w_2) essentially make this a “tri-Maxwellian.” In general, we utilize $w_2 > w_1$ to produce a positive heat flux along the parallel axis. This gives rise to a positive first moment $u_r = (w_2 - w_1)/\sqrt{\pi}$ which must be taken into account when computing $\mathbf{c} = \mathbf{v} - \mathbf{u}$ for the higher moments. We do not plot an example of this VDF in Figure 1 because its contours look almost the same as the skew-normal distribution discussed below. The skewness inherent in equation (39) can be parameterized by a dimensionless asymmetry parameter $\sigma_t = (w_2/w_1) - 1$. In order for the pressure to be isotropic (i.e., for \mathcal{P}_{rr} to remain equal to $\mathcal{P}_{\theta\theta}$ and $\mathcal{P}_{\phi\phi}$), we must also set

$$w_0^2 = \left[\frac{(\sigma_t + 1)^3 + 1}{\sigma_t + 2} - \frac{2\sigma_t^2}{\pi} \right] w_1^2, \quad (40)$$

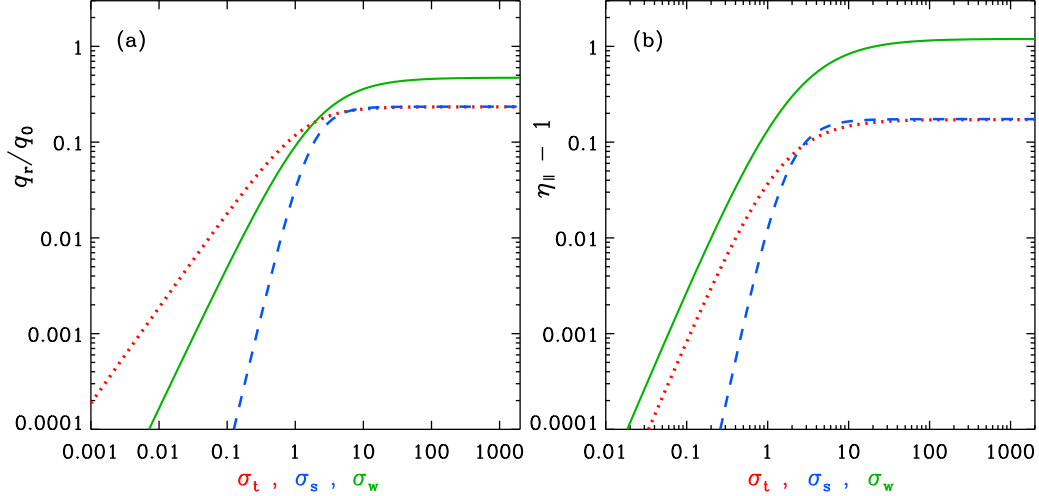


Figure 2. (a) Normalized heat flux q_r/q_0 plotted as a function of skewness parameters σ_t (for the two-sided bi-Maxwellian VDF; red dotted curve), and σ_s (for the skew-normal VDF; blue dashed curve), and σ_w (for the BGK Wheelton & Woo VDF; green solid curve). (b) Fourth-order moment coefficient ($\eta_{\parallel} - 1$) plotted as a function of the same skewness parameters shown in panel (a).

and it is clear that for $\sigma_t = 0$, the parameters reduce to $w_0 = w_1 = w_2$.

We solved for the zeroth through fourth moments of this two-sided VDF using a numerical code that simulates the full three-dimensional velocity space using discrete grids of no less than 1000 points in v_r , v_{θ} , and v_{ϕ} , with bounds of $\pm 10w_0$ along each axis. Figure 2a shows the resulting parameter dependence of q_r/q_0 as a function of σ_t . For small values of the asymmetry parameter, q_r/q_0 increases linearly with σ_t , then it saturates to a maximum value as $\sigma_t \rightarrow \infty$. In this asymptotic limit, the VDF is essentially just one-sided or hemispherical; i.e., the $v_{\parallel} > 0$ bi-Maxwellian piece is present, but the $v_{\parallel} < 0$ piece has collapsed to a thin sheath around $v_{\parallel} \approx 0$. The limiting value for the heat flux can then be evaluated analytically, and it is given exactly by

$$\max\left(\frac{q_r}{q_0}\right) = \frac{4 - \pi}{3(\pi - 2)^{3/2}} \approx 0.234588. \quad (41)$$

Note that for all values of σ_t , the heat-flux tensor is partitioned such that

$$\alpha_{\parallel} = 1, \quad \alpha_{\perp} = 0, \quad (42)$$

which is quite different from the Grad-expansion coefficients given in equation (37).

For the fourth-order moments, we found that $\eta_{\perp} = 1$ for all values of σ_t , but η_{\parallel} is an increasing function of σ_t . Figure 2b shows this dependence on the asymmetry parameter. For low values of σ_t , $\eta_{\parallel} \approx 1$ as it should be for a non-skewed Maxwellian. For high values of σ_t , η_{\parallel} saturates at a value of about 1.1738.

3.4 Skew-Normal Distributions

Originally developed by O'Hagan & Leonard (1976), the skew-normal distribution is a generalization of the normal (Gaussian) distribution to nonzero values of the third moment. This distribution has been applied in many fields (see, e.g., Azzalini & Capitanio, 2014) and it has been used to model particle VDFs in systems under the influence of specific types of magnetized Hamiltonians (Yamaguchi, 2015).

As above, we write the proposed VDF in a frame in which the bulk flow speed is zero in the limit of no skewness:

$$f(\mathbf{v}) = \frac{n}{\pi^{3/2} w_{\parallel} w_{\perp}^2} \exp\left(-\frac{v_{\parallel}^2}{w_{\parallel}^2} - \frac{v_{\perp}^2}{w_{\perp}^2}\right) \left[1 + \operatorname{erf}\left(\frac{\sigma_s v_{\parallel}}{w_{\parallel}}\right)\right], \quad (43)$$

where erf is the Gaussian error function and σ_s is a skewness parameter similar to σ_t from the previous section, in that the limit of $\sigma_s = 0$ represents zero skewness, and thus zero heat flux. When $\sigma_s > 0$, there is a nonzero bulk flow speed

$$u_r = \frac{\sigma_s w_{\parallel}}{\sqrt{\pi(1 + \sigma_s^2)}} \quad (44)$$

and the pressure tensor can be made isotropic if the following condition on the second moments is imposed:

$$w_{\perp}^2 = w_{\parallel}^2 \left[1 - \frac{2\sigma_s^2}{\pi(1 + \sigma_s^2)}\right]. \quad (45)$$

Figure 1b shows an example set of contours for this VDF, once the isotropization has been imposed, and we note that it looks very similar to the two-sided bi-Maxwellian from Section 3.3.

We solved for the higher moments using the same numerical code as discussed above, and we show in Figure 2a how q_r/q_0 depends on σ_s . In the low-skewness limit, q_r/q_0 increases quite steeply, in proportion to σ_s^3 . In the high-skewness limit, the VDF approaches the same shape as the two-sided bi-Maxwellian, so q_r/q_0 approaches the same limiting value of 0.234588. For all values of σ_s , the heat-flux tensor also has the same partitioning behavior as the VDF from Section 3.3, with $\alpha_{\parallel} = 1$ and $\alpha_{\perp} = 0$. There is also similar behavior for the fourth moments, with $\eta_{\perp} = 1$ for all values of the skewness, and the same maximum value of $\eta_{\parallel} = 1.1738$. Figure 2b shows how the approach to this value differs from the two-sided bi-Maxwellian case, though.

3.5 Electrostatic BGK Solutions

When studying the kinetic properties of a moderately ionized plasma subject to an electric field, Whealton & Woo (1972) found an elegant solution to the Boltzmann transport equation. By making use of the constant collision-time approximation of Bhatnagar et al. (1954), hereafter BGK, they found an analytic solution that carries a nonzero heat flux without any regions of negative VDF. In terms of a dimensionless skewness parameter σ_w , we can write this distribution as

$$f(\mathbf{v}) = \frac{n\Sigma}{2\pi e w^3} \exp\left(-\frac{v_{\perp}^2}{w^2} - \frac{v_{\parallel}\Sigma}{w} + \frac{1}{\sigma_w}\right) \operatorname{erfc}\left[\frac{1}{\sqrt{\sigma_w}} - \frac{\sqrt{\sigma_w}}{2}\left(1 + \frac{v_{\parallel}\Sigma}{w}\right)\right], \quad (46)$$

where $\Sigma = \sqrt{(4 + 2\sigma_w)/\sigma_w}$ and erfc is the complementary error function. When $\sigma_w \rightarrow 0$, this distribution reduces to an isotropic Maxwellian. Applications of this VDF to the solar wind have been proposed by Leblanc & Hubert (1997, 1998), and Figure 1c illustrates its shape.

The above form for $f(\mathbf{v})$ is convenient for analysis, since its first moment automatically integrates to $u_r = 0$ no matter the value of σ_w , and its second-moment pressure-tensor components are always isotropic. For the third moment, Figure 2a shows how the numerically computed values of q_r/q_0 approach a constant asymptotic value for large values of σ_w , and this value is different than the ones discussed above. In this case, the $\sigma_w \rightarrow \infty$ limit produces a truncated exponential function along the parallel-velocity axis, with

$$f(\mathbf{v}) \approx \frac{n\sqrt{2}}{\pi e w^3} \exp\left(-\frac{v_{\perp}^2}{w^2} - \frac{v_{\parallel}\sqrt{2}}{w}\right) H(v_{\parallel} + w/\sqrt{2}), \quad (47)$$

and the Heaviside step function $H(x)$ is used to indicate that the asymptotic distribution function is zero for all $v_{\parallel} < -w/\sqrt{2}$. For this distribution, $q_r/q_0 = \sqrt{2}/3 \approx 0.4714$, almost exactly twice the limiting value for the two-sided bi-Maxwellian and skew-normal VDFs.

For all values of σ_w , the Wheelton & Woo (1972) distribution exhibits $\alpha_{\parallel} = 1$ and $\alpha_{\perp} = 0$. This type of third-moment partitioning seems to be ubiquitous for VDFs that are separable functions of a skewed one-dimensional distribution in the parallel direction and a Gaussian function in the perpendicular direction. The fourth-moment behavior of this VDF is also similar to the distributions discussed in Sections 3.3–3.4, since $\eta_{\perp} = 1$, and η_{\parallel} increases monotonically as a function of the skewness parameter σ_w as shown in Figure 2b. The maximum value of η_{\parallel} in this case is 11/5.

3.6 Multi-Component Fits to Data

Analytic parameterizations of VDF skewness can be of great pedagogical interest, but we also want to ensure that our models resemble the electron distributions actually observed in the solar wind. Thus, we sought high-precision functional fits to the core, halo, and strahl components of electron VDFs measured at specific times. When the centroids of these components drift relative to one another, they correspond to nonzero heat fluxes. These VDFs have been measured, split into components, and fit with various functions for several decades (see, e.g., Štverák et al., 2009). For the purposes of this paper, we focused on publicly available data, based on statistically robust fitting procedures, that retain the precision needed to compute third-order and fourth-order moments. The two sources we used are described as follows:

1. Wilson et al. (2019a) performed multi-parameter fits to a set of 15,314 electron VDF measurements made at 1 AU, between 1995 and 2000, with the *Wind* spacecraft’s 3DP low-energy electrostatic analyzer. These data were selected for proximity to known interplanetary shocks, but several statistical features were found to be similar to known trends in the ambient solar wind (see also Wilson et al., 2019b, 2020). Out of that entire data set, we identified a subset of 2,840 measurements that had the highest-quality fit-flag ratings and nonzero values of the relevant number densities. We used the fit parameters provided in the online dataset of Wilson et al. (2019a) and reconstructed the VDFs using their specified bi-Maxwellian, bi-kappa, and bi-self-similar fitting functions. Figure 1d shows an example VDF reconstruction that corresponds to one of the largest measured values of q_r/q_0 .
2. Scherer et al. (2021) provided two examples of multicomponent VDF fits made with data from the *Ulysses* SWOOPS (Solar Wind Observations Over the Poles of the Sun) instrument, from days 288 and 365 of the year 2002. This was a time period when *Ulysses* was in the ambient solar wind at heliocentric distances between 4.2 and 4.5 AU. The fitting functions included drifting bi-Maxwellians and generalized anisotropic κ distributions.

We computed full sets of moments for each VDF using a similar numerical code to the one that produced the results shown in Figure 2. Because the measured heat fluxes are sometimes oriented in the sunward direction, and sometimes anti-sunward, we took absolute values of q_r in order to treat both cases on equal footing. The full range of computed q_r/q_0 ratios for the Wilson et al. (2019a) data spanned more than three orders of magnitude, from 1.02×10^{-4} to 0.209. The mean of the distribution of 2,840 values was 0.0470, and the corresponding median was 0.0379, with one-standard-deviation bounds (i.e., 16% and 84% percentiles) at values of 0.0139 and 0.0879. The two Scherer et al. (2021) models had large normalized heat flux values of 0.2003 and 0.3201. These values appear consistent with other statistical studies of the electron heat flux at 1 AU (e.g., Salem et al., 2003; Bale et al., 2013).

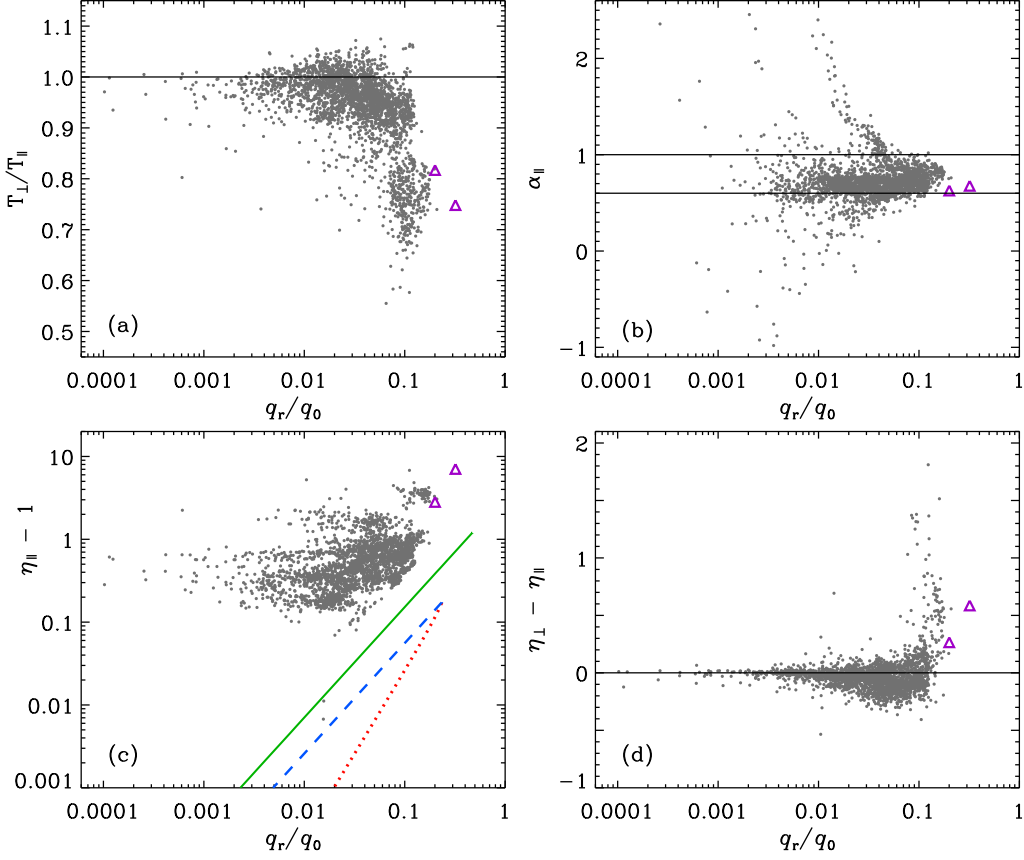


Figure 3. Dimensionless moment quantities for measured VDFs of Wilson et al. (2019a) (gray dots) and Scherer et al. (2021) (purple triangles) plotted versus normalized heat flux q_r/q_0 . (a) Anisotropy ratio T_{\perp}/T_{\parallel} , with the isotropic value of 1 highlighted by a horizontal line. (b) Third moment partition fraction α_{\parallel} , with analytic values (0.6, 1) highlighted by lines. (c) Fourth moment quantity ($\eta_{\parallel} - 1$), with analytic results shown with curves of same colors/styles of Figure 2. (d) Fourth moment difference ($\eta_{\perp} - \eta_{\parallel}$).

Figure 3a shows that the electron anisotropy ratio $T_{\perp}/T_{\parallel} = \mathcal{P}_{\theta\theta}/\mathcal{P}_{rr}$ is generally near unity for solar-wind electrons at 1 AU. The median of the distribution of the Wilson et al. (2019a) values is 0.959, with ± 1 standard deviation bounds at values of 0.87 and 1.01. The two Scherer et al. (2021) models are on the more anisotropic side, with $T_{\perp}/T_{\parallel} = 0.748$ and 0.817. Despite these anisotropy ratios not being exactly equal to one, they seem sufficiently close that the results for the third-order and fourth-order moments ought to be at least roughly comparable to the isotropized analytic models of Sections 3.2–3.5.

Figure 3b shows how the third-order partition fraction α_{\parallel} does not seem to depend strongly on the value of the heat flux. The larger spread at lower values of q_r/q_0 may be the result of fitting uncertainties when the skewness is weak, but it is notable that the other panels of Figure 3 do not show this kind of spread at low q_r/q_0 . The median of the distribution of plotted values of α_{\parallel} is 0.704, with ± 1 standard deviation limits between 0.59 and 0.83. Note that roughly three-quarters of the plotted values (i.e., 2,175 out of 2,840) fall in between the analytic values corresponding to the Grad-expansion VDFs ($\alpha_{\parallel} = 0.6$) and the other analytic VDFs ($\alpha_{\parallel} = 1$). The two Scherer et al. (2021) cases have $\alpha_{\parallel} = 0.628$ and 0.677.

Figure 3c shows the fourth-order moment quantity η_{\parallel} alongside the three sets of analytic trends from Figure 2. For both sets of measured data, the full range of η_{\parallel} values extends from 1.007 to 8.05. There is a hint of a trend of positive correlation with q_r/q_0 (like in the analytic models), but it is not a strong trend. It may then be reasonable to just adopt the median value ($\eta_{\parallel} = 1.492$) for the data in future modeling efforts. Note that the existence of κ tails in the measured VDFs gives rise to larger values of the fourth moment than were found in the analytic VDF models discussed above. This was anticipated in equation (35).

Figure 3d shows that η_{\perp} tends to remain close to η_{\parallel} , with a median value of their difference being only $(\eta_{\perp} - \eta_{\parallel}) = -0.033$. Note, however, that the median of the distribution of η_{\perp} values themselves is 1.444, which corresponds to a slightly different value of the difference when the two medians are subtracted. One can also see that, even though these median differences are negative, the cases of strongest heat flux—including the two VDFs described by Scherer et al. (2021)—tend to have positive values. Thus, in some situations it may be appropriate to just adopt $\eta_{\perp} = \eta_{\parallel}$, which simplifies the equations for q_r .

4 Applicability to the Solar Wind

Although the results of Sections 2 and 3 are interesting on their own, we would like to also begin exploring solutions for q_r with ambient plasma conditions relevant to the observed solar wind. However, the solutions presented below should be considered only as example cases that scratch the surface of how equations (18)–(22) can be applied once one adopts particular values for the VDF-specific third-order and fourth-order constants. For example, several eight-moment and gyrotropic models of the solar wind (Olsen & Leer, 1996, 1999; Schiff, 2020) used the values from the Grad-type (Schunk, 1977) expansion:

$$\{\alpha_{\parallel}, \alpha_{\perp}, \eta_{\parallel}, \eta_{\perp}\} = \{0.6, 0.4, 1, 1\} \quad (48)$$

(see also Blelly & Schunk, 1993; Li, 1999; Lie-Svendson et al., 2001; Kuznetsov & Dzhaliylov, 2009). We will also explore the implications of using the median values derived from *Wind* data and discussed in Section 3.6:

$$\{\alpha_{\parallel}, \alpha_{\perp}, \eta_{\parallel}, \eta_{\perp}\} = \{0.704, 0.296, 1.492, 1.444\} . \quad (49)$$

Section 4.1 examines some potentially useful closed-form limiting cases, Section 4.2 presents numerical solutions, and Section 4.3 discusses how things change if we include external source/sink terms in the conservation equations.

4.1 Analytic Scaling Relations

Although the specification of q_r in equations (20)–(22) is the most general result of this paper, we find it useful to work with a simplified version that can be applied in much of the solar wind. Sufficiently far from the Sun, the solar wind has accelerated to a nearly constant speed (so that $\partial u_r / \partial r \approx 0$) and the expansion is close to spherically symmetric (so that $A \propto r^2$ and $L_A \approx r/2$). In that case, mass-flux conservation demands that $n \propto r^{-2}$ and we can parameterize the radial dependence of electron temperature as $T \propto r^{-\delta}$. This gives

$$q_r \approx \frac{pu_r^2(4 - 3\delta) + 5pw^2(\eta_{\perp} + \delta\eta_{\parallel} - 1 - \delta/2)}{4\alpha_{\perp}u_r + 2\nu_{\text{eff}}r} . \quad (50)$$

In the weak-skewness limit of $\eta_{\parallel} \approx \eta_{\perp} \approx 1$, the second expression in parentheses above reduces to $\delta/2$, and Section 2.3 showed how ν_{eff} can be defined with a normalizing constant $\xi = 0.8325$. However, for other values of η_{\parallel} and η_{\perp} , one would have to use

$$\xi = 0.8325 \left(\frac{\eta_{\perp} + \delta\eta_{\parallel} - 1 - \delta/2}{\delta/2} \right) \quad (51)$$

in order to ensure Spitzer & Härm (1953) conductivity in the limit of rapid collisions for a static ($u_r = 0$) plasma.

If we assume that collisions are weak and the electron temperature is roughly constant with distance (i.e., $\delta \approx 0$), together with the approximation $\eta_\perp \approx 1$, then equation (50) reduces to

$$q_r \approx \frac{pu_r}{\alpha_\perp}, \quad (52)$$

which is essentially the free-streaming limit derived by Hollweg (1974, 1976):

$$q_r \approx \frac{3}{2}\alpha_H u_r n k_B T = \frac{3}{2}\alpha_H p u_r. \quad (53)$$

Typical values of α_\perp of 0.3–0.4 give a predicted range for Hollweg’s constant α_H of 1.7–2.2. This falls within the somewhat broader range of likely values ($1 < \alpha_H < 4$) discussed by Hollweg (1974, 1976).

As shown below, the limit of $\delta \approx 0$ is not often seen in the solar wind. For realistic temperature gradients and outflow speeds, the first (u_r^2 dependent) term in the numerator of equation (50) tends to be much smaller in magnitude than the second (w^2 dependent) term in much of the heliosphere. In that case, the limit of weak collisions would provide a heat flux that scales as

$$q_r \propto \frac{pw^2}{u_r}, \quad (54)$$

with a dimensionless multiplicative constant (depending on α_\perp , δ , η_\parallel , and η_\perp) left unwritten. This type of collisionless heat-flux relation does not resemble either the free-streaming limit ($q_r \propto pu_r$) or the saturated limit ($q_r \propto pw$). Note that there is no combination of terms in the numerator and denominator of equation (50) that yields the well-studied saturated limit of $q_r \approx q_0$. Halekas et al. (2021) found an approximate anti-correlation between the heat flux and the solar wind speed in data from *Parker Solar Probe* (PSP), which may support scaling relations like equation (54).

Equation (50) resembles a frequently-used way of specifying a gradual transition from collisional to collisionless heat flux in solar-wind simulations. For example, Cranmer et al. (2007) followed Wang (1993) and others to adopt a form that was given as

$$q_r = \frac{\nu_{\text{exp}} q_{\text{FS}} + \nu_{\text{coll}} q_{\text{SH}}}{\nu_{\text{exp}} + \nu_{\text{coll}}}, \quad (55)$$

where q_{SH} is the Spitzer-Härm heat flux, q_{FS} is an estimate of the free-streaming (collisionless) heat flux taken from Hollweg (1974, 1976), $\nu_{\text{coll}} \approx \nu_{\text{eff}}$ is an electron self-collision frequency, and ν_{exp} is a local rate of solar-wind expansion. When these terms are translated into the notation of this paper, this expression becomes

$$q_r \approx \frac{3\alpha_H p u_r^2 + 1.59\delta p w^2}{2u_r + 1.28\nu_{\text{eff}} r}, \quad (56)$$

which closely resembles equation (50) above. Heat-flux formulations like equation (55) are intended to be strongly collisional near the Sun (where $\nu_{\text{coll}} \gg \nu_{\text{exp}}$) and collisionless far from the Sun (where $\nu_{\text{coll}} \ll \nu_{\text{exp}}$). However, these expected radial variations in the relative values of ν_{coll} and ν_{exp} may not be so straightforward. In the denominator of equations (50) and (56), the $\nu_{\text{eff}} r$ term may either increase or decrease with increasing r , depending on the value of δ . Specifically, $\nu_{\text{eff}} r \propto r^{(3\delta-2)/2}$, so it only grows weaker with distance when $\delta < 2/3$.

4.2 Representative Numerical Models

To illustrate the behavior of the modeled heat flux as a function of heliocentric distance, we evaluated equations (20)–(22) numerically using tabulated models of solar-wind

plasma properties. The outflow speed u_r , number density n , and flux-tube area expansion factor A were taken from a semi-empirical model of the time-steady fast solar wind (Cranmer & van Ballegoijen, 2012). For the electron temperature T , we wanted to vary the radial exponent δ as a free parameter, so we used the analytic model described further in the Appendix. In all cases shown below, the following parameters of that model were fixed: $T_{\max} = 1.35$ MK, $\psi = 4.5$, and the latter is consistent with a dimensionless height of the temperature maximum of $x_{\max} = 1.842$. These values were chosen to match a recent set of collected observations of the electron temperature above polar coronal holes (Cranmer, 2020).

Figure 4a shows a range of electron temperature models, with δ varied between 0.1 and 1 in steps of 0.1. Measured values from the solar wind come from *PSP* (Halekas et al., 2020), *Helios* (Maksimovic et al., 2020), and *Ulysses* (Bame et al., 1992; Goldstein et al., 1996), with the processing of the latter two sources discussed in more detail by Cranmer et al. (2009). For these data, the best-fitting value of δ seems to be about 0.6. Note that at 1 AU, an electron temperature of $\sim 10^5$ K corresponds to $w \approx 1,750$ km s⁻¹, which is significantly larger than typical solar-wind speeds of $u_r \approx 300$ –700 km s⁻¹.

Figure 4b shows corresponding solutions to equations (20)–(22) for the median parameter values given in equation (49). To compute the collision rate ν_{eff} , we needed to evaluate the Coulomb logarithm,

$$\ln \Lambda = 23.2 + \frac{3}{2} \ln \left(\frac{T}{10^6 \text{ K}} \right) - \frac{1}{2} \ln \left(\frac{n}{10^6 \text{ cm}^{-3}} \right). \quad (57)$$

Also shown are measured values from *PSP* (Halekas et al., 2021), *Helios* (Pilipp et al., 1990), and *Ulysses* (Scime et al., 2001), and it is clear that the best-fitting temperature exponent of $\delta = 0.6$ also appears to produce heat fluxes that agree somewhat well with the data. Note that the radial distance where $q_r = 0$ occurs at slightly different places in the low corona, depending on the value of δ , and it never coincides exactly with the location where $\partial T / \partial r = 0$. Below, we discuss comparisons between these numerical calculations and the limiting cases of Spitzer-Härm heat flux (q_{SH}) and saturated heat flux (q_0).

In Figure 4c, we fix δ at its best-fitting value of 0.6 and explore what happens when the higher-moment parameters (α_{\parallel} , α_{\perp} , η_{\parallel} , η_{\perp}) are varied. The curves in Figure 4c represent 10 different selections of parameters from the list of 2,840 cases in the Wilson et al. (2019a) database. Generally, larger values of α_{\parallel} (i.e., smaller values of α_{\perp}) corresponded to larger values of q_r at 1 AU, but no definitive correlations were seen with the η_{\parallel} or η_{\perp} parameters. Note that even when holding δ fixed, the radial distance where $q_r = 0$ can vary, depending on the values of the higher-moment parameters. It is clear that the electron heat flux in interplanetary space depends on both macroscopic properties of the expansion (i.e., δ) and microscopic properties of the skewed electron VDF.

Figure 5 shows modeled values of the ratio q_r/q_0 at a fixed distance of $r = 1$ AU, plotted versus the dimensionless Knudsen number that is defined as

$$\text{Kn} = \frac{w}{\nu_{\text{eff}}} \left| \frac{\partial \ln T}{\partial r} \right|. \quad (58)$$

Here, we use the fixed value of $\xi = 0.8325$ in the definition for ν_{eff} in order to have a single consistent scale. Traditionally, values of $\text{Kn} \ll 1$ denote strongly collisional regimes and values of $\text{Kn} > 1$ denote collisionless regimes. Note that the range of plotted Kn values is slightly larger than the typical observed range (Salem et al., 2003; Bale et al., 2013). This is probably because the bulk outflow speed and density in our models were specified for the fast solar wind, which tends to be less collisional than the slow solar wind.

The curves in Figure 5 represent finer grids of δ values than were shown in Figure 4, and we also selected three different sets of higher-moment constants: those from equations (48) and (49), and one with $\alpha_{\parallel} = 0$ and $\eta_{\parallel} = \eta_{\perp} = 1$ to illustrate the lowest

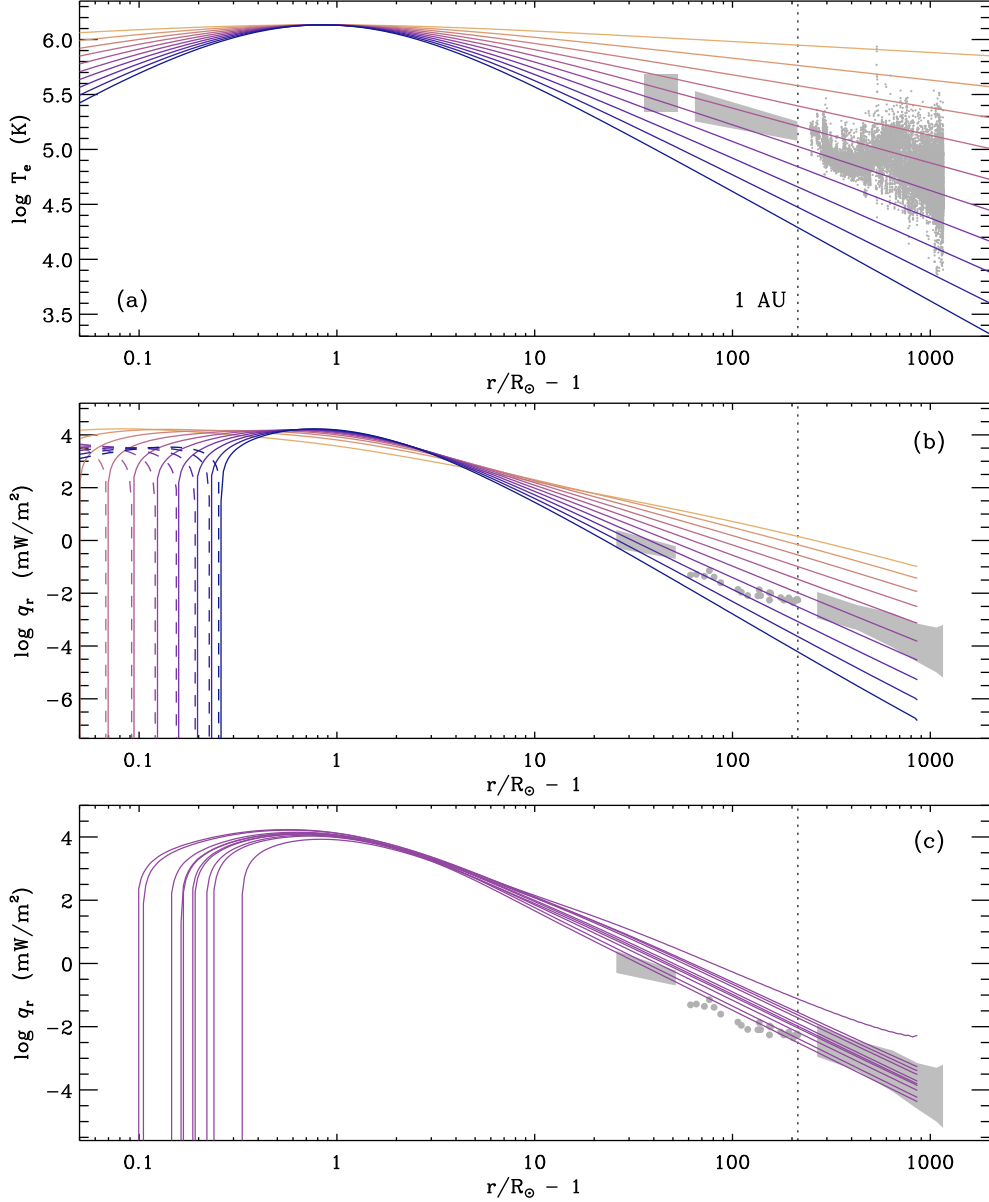


Figure 4. (a) Radial dependence of electron temperature for analytic models (solid curves) and in situ data (gray regions). Curve colors go from gold ($\delta = 0.1$) to violet ($\delta = 1$). (b) Computed values of q_r for temperatures shown in panel (a), using equation (49), also compared with in situ data. Solid curves show $q_r > 0$, and dashed curves show $|q_r|$ when $q_r < 0$. (c) Computed values of q_r for the $\delta = 0.6$ model and a selection of higher-moment constants from the Wilson et al. (2019a) database, with negative values not shown.

heat fluxes that are likely to be obtained from this model. In this kind of diagram, the Spitzer-Härm limit is a straight line, with $|q_{\text{SH}}|/q_0$ varying linearly with Kn. The order-unity normalization factor between these two quantities is often given as 1.07, but its precise value depends on details of how the Coulomb collision rates and mean-free paths are defined. Using the definitions given above, that factor here is 0.833.

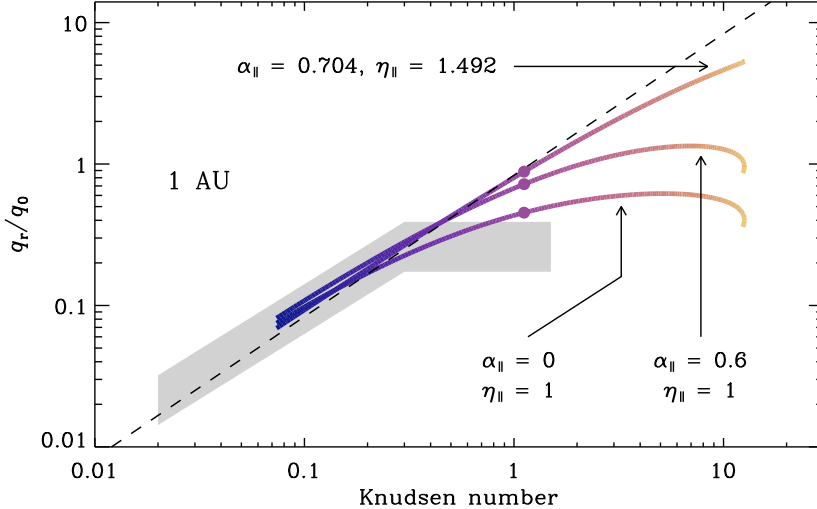


Figure 5. Normalized heat flux ratio q_r/q_0 at 1 AU plotted versus Knudsen number, for three sets of higher-moment constants (see text). Solid curves denote values modeled with a fine grid of temperature gradients, from $\delta = 0.1$ (gold) to $\delta = 1$ (violet), with the best-fitting value of $\delta = 0.6$ highlighted with circles. Also shown: q_{SH}/q_0 (black dashed curve) and an approximate range of measured data from *Wind* (Bale et al. (2013); gray region).

Although the model curves shown in Figure 5 do not agree perfectly with the data, it is interesting that they still show a similar trend of dipping below the Spitzer-Härm value at the largest Knudsen numbers. We also note, following Landi et al. (2014), that just because a point may happen to be near the linear q_{SH}/q_0 relationship on this diagram, it does not mean that the corresponding heat flux is well-described by classical Spitzer & Härm (1953) conductivity. In reality, we expect that kinetic instability thresholds (that are not yet included in our model) must be responsible for limiting the observed heat fluxes to values below $q_r/q_0 \approx 0.3$ – 0.4 ; see Section 5 below.

4.3 Effects of External Sources and Sinks

The conservation equations for electron VDF moments do not exist in a vacuum. As mentioned in Section 2.1, there are several ways that other particle species and external forces can give rise to additional terms in these equations. For example, in the momentum equation, electrons feel the effects of gravity (inward), MHD-wave pressure (outward), and the Lorentz force associated with a charge-separation electric field (usually inward for electrons). In the thermal energy equation, there can be multiple competing sources of heating and cooling from collisions, radiation, or wave-particle interactions.

In order to explore the importance of these source/sink terms to the determination of the electron heat flux, we can add an arbitrary vector momentum density \mathbf{M} to the right-hand side of equation (7) and a scalar heating term Q to the right-hand side of equation (8). If we also rewrite the momentum source as $\mathbf{M} = m n \mathbf{a}$, where \mathbf{a} is an acceleration, then these terms can be carried through to the analytic solution given by equations (20)–(22). In that solution, we would replace q_{num} by \tilde{q}_{num} , and the latter is defined as

$$\tilde{q}_{num} = q_{num} - \frac{2}{5} u_r Q - p a_r . \quad (59)$$

Note that both new terms are negative, since the presence of local sources of electron momentum or energy would reduce the need for radial heat flux to have to transport energy out to maintain a given steady state.

There have been several estimates of the magnitude of the electron heating rate Q in the solar wind. Vasquez et al. (2007), Cranmer et al. (2009), and Stawarz et al. (2009) found values between roughly 10^{-17} and 10^{-16} W m^{-3} at 1 AU. This range would produce terms in equation (59) of order 10^{-12} to 10^{-11} $\text{W m}^{-2} \text{s}^{-1}$. However, the $\delta = 0.6$ model of Figure 4b exhibited a value of $q_{\text{num}} \approx 10^{-10}$ $\text{W m}^{-2} \text{s}^{-1}$ at 1 AU. Thus, these heating terms may only be 1% to 10% corrections to the electron heat flux computed without them. In addition, Štverák et al. (2015) concluded that the uncertainties inherent in many observational determinations of the electron heating rate may be high enough that we are not even sure whether Q is positive or negative at 1 AU. Thus, we defer further discussion of these source/sink terms (including the a_r term) to future work.

5 Discussion and Conclusions

It is a long-standing goal of heliophysics to produce self-consistent models of coronal heating, solar wind acceleration, and the multi-scale structure of the heliosphere. If such models are to employ fluid-based conservation equations for the moments of electron, proton, and heavy-ion VDFs, it is necessary for those equations to be free from overly limiting or inconsistent assumptions about the kinetic microphysics. For example, we have known for decades that it is inappropriate to use the classical Spitzer-Härm heat flux in regions with infrequent collisions. There are also major problems with using polynomial VDF expansions that provide collisionless expressions for heat flux at the expense of creating large regions of unphysically negative phase-space density. Thus, in this paper we have attempted to navigate this minefield by investigating multiple ways of expressing heat-flux-carrying skewness in a model electron VDF, and then exploring how each kind of skewed distribution affects the higher-moment conservation equations for the heat flux itself.

Much of the effort in this paper was devoted to computing values for the third-moment ($\alpha_{\parallel}, \alpha_{\perp}$) and fourth-moment ($\eta_{\parallel}, \eta_{\perp}$) partition fractions needed to specify all terms in the heat-flux conservation equation. Both idealized analytic VDFs (Sections 3.3–3.5) and fits to measured solar-wind electron data (Section 3.6) showed roughly similar ranges of likely values for the partition fractions. Further work is definitely needed to produce optimally customized sets of parameters for use in models of specific regions of the heliosphere. However, it is interesting that the higher-moment parameters of the flawed Grad-type expansion technique (Section 3.2) were not *too* far removed from the other values computed for positive-definite VDFs. This suggests that some results of eight-moment and gyrotropic models of the solar wind may yet have value despite their being built on somewhat shaky foundations.

To improve our current descriptions of electron heat flux, it is clear that more kinetic theory is needed. In recent years, insights from collisionless exospheric approaches to the solar wind have begun to be appreciated more by the fluid-based modeling community (see, e.g., Echim et al., 2011; Viall & Borovsky, 2020). There may also be specific kinetic connections between the solar atmosphere and heliosphere that depend on the physics of coronal heating; i.e., nanoflare-generated beams that can affect the electron strahl and halo in the heliosphere (Che & Goldstein, 2014). Perhaps most importantly, the effects of kinetic instabilities must also be included when attempting to determine the electron heat flux in interplanetary space (Forshund, 1970; Perkins, 1973; Gary et al., 1975; Scime et al., 1994; Shaaban et al., 2018; Tong et al., 2019; Innocenti et al., 2020; López et al., 2020; Micera et al., 2020).

It is possible that new analytic forms of skewed VDFs can be constructed that represent observed heat-flux trends better than the ones discussed in this paper. Parameterizations that treat the electron strahl as a narrow beam in velocity space (e.g., Horaites et al., 2018) or as a truncated bi-kappa function (Štverák et al., 2009) may be particularly useful. Alternative moment-closure ideas, such as maximum entropy constraints (Levermore, 1996; Groth & McDonald, 2009), perturbative expansions that go to higher orders (Mintzer, 1965; Struchtrup & Torrilhon, 2003; García-Colín et al., 2008), or spatially nonlocal treatments that scale with the mean-free path (Luciani et al., 1983; Canullo et al., 1996) could be helpful as well. Lastly, we note that collisionless modifications to the heat flux carried by electrons may be important in astrophysical contexts far beyond our heliosphere (see, e.g., Cowie & McKee, 1977; Narayan & Medvedev, 2001; Voit, 2011).

Appendix A Analytic RTV-like Temperature Laws for the Solar Wind

For time-steady heating, the solar corona usually exhibits a time-steady solution for temperature and density as a function of spatial position. Rosner et al. (1978), hereafter RTV, produced analytic and semi-analytic solutions for closed coronal loops (see also Serio et al., 1981; Aschwanden et al., 2001). Martens (2010) showed that, for a specific way of parameterizing the heating rate, the dependence of temperature on position can be written using the inverse of an incomplete beta function. However, for the open field lines that connect the Sun to the heliosphere, there do not seem to be closed-form solutions of this kind. Schwadron & McComas (2003) laid out some necessary ingredients for such a calculation, but no analytic solutions for $T(r)$ were found. In this appendix we reproduce a derivation, originally given by Schiff (2020), for a closed-form solution to a simplified version of the thermal energy conservation equation in an open-field geometry.

Normally, the solution of the thermal energy equation in the corona is a balance between terms describing direct heating, thermal conduction, radiative losses, and enthalpy transport due to flows. Bradshaw et al. (2019) found that accounting for only a subset of these terms can still produce reasonable solutions at times. Let us assume, for the low corona and upper transition region, that the radiative losses are negligible (because the electron density begins to decrease rapidly with increasing height) and that the enthalpy transport terms are also negligible (because the solar wind has not yet accelerated to high speeds). In that case, the time-steady energy balance contains only terms describing direct heating and thermal conduction:

$$Q_{\text{heat}} + Q_{\text{cond}} = 0, \quad (\text{A1})$$

where the Q terms are volumetric energy deposition rates in the same units as the terms in equation (12). Describing the heating using a power-law function of heliocentric distance r (see, e.g., Hu et al., 1997; Cranmer et al., 2009), we can write

$$Q_{\text{heat}} = Q_{\odot} \left(\frac{R_{\odot}}{r} \right)^{\psi} \quad (\text{A2})$$

where Q_{\odot} is a normalizing constant that sets the rate of heating at the base of the corona, and ψ describes its power-law rate of radial decrease. For simplicity, let us describe the thermal conduction using the Spitzer-Härm limit in spherical geometry, with

$$Q_{\text{cond}} = \frac{\kappa_0}{r^2} \frac{d}{dr} \left(r^2 T^{5/2} \frac{dT}{dr} \right). \quad (\text{A3})$$

If we make the following change of variables,

$$x = \frac{r}{R_{\odot}}, \quad y = \left(\frac{T}{T_{\text{max}}} \right)^{7/2} \quad (\text{A4})$$

then equation (A1) can be written as

$$\frac{\zeta}{x^\psi} + \frac{1}{x^2} \frac{d}{dx} \left(x^2 \frac{dy}{dx} \right) = 0, \quad (\text{A5})$$

where the dimensionless constant ζ is given by

$$\zeta = \frac{7R_\odot^2 Q_\odot}{2\kappa_0 T_{\max}^{7/2}}. \quad (\text{A6})$$

Note that we have introduced an additional unknown parameter into the system: the peak coronal temperature T_{\max} . Following Rosner et al. (1978), we realize that *overspecifying* the boundary conditions can lead to the ability to solve for not only this new parameter, but also for the radial distance x_{\max} at which $T = T_{\max}$. Equation (A5) is a second-order differential equation, which requires specifying only two boundary conditions on the desired solution for $y(x)$. However, let us specify four such conditions:

$$y(1) = 0, \quad y(x_{\max}) = 1, \quad y'(x_{\max}) = 0, \quad y(\infty) = 0. \quad (\text{A7})$$

In other words, we assume the chromospheric lower boundary at $x = 1$ is sufficiently “cold” such that $T \ll T_{\max}$, and that the temperature also asymptotes to zero at large enough distances from the Sun. Also, we assume that the height x_{\max} at which the temperature reaches its peak is a well-behaved local maximum where the first derivative of y is equal to zero.

Depending on the value of the exponent n , there are three possible closed-form solutions to equation (A5). There are special cases for $\psi = 2$ and $\psi = 3$, as well as a general solution,

$$y(x) = \frac{C_1}{x} + C_2 - \frac{\zeta x^{2-\psi}}{\psi^2 - 5\psi + 6} \quad (\text{A8})$$

where C_1 and C_2 are constants that must be fixed by applying the boundary conditions, and this expression does not hold for either $\psi = 2$ or $\psi = 3$. The boundary conditions on $y(1)$ and $y(\infty)$ demand that

$$C_1 = \frac{\zeta}{\psi^2 - 5\psi + 6}, \quad C_2 = 0 \quad (\text{A9})$$

and the other boundary conditions help to determine

$$x_{\max} = (\psi - 2)^{1/(\psi-3)}, \quad \zeta = (\psi - 2)^{(2\psi-5)/(\psi-3)}. \quad (\text{A10})$$

This yields a closed-form solution given by

$$y(x) = \frac{(\psi - 2)^{(\psi-2)/(\psi-3)}}{\psi - 3} \left(\frac{1}{x} - \frac{1}{x^{\psi-2}} \right). \quad (\text{A11})$$

As mentioned above, the overspecification of boundary conditions also allows a numerical value of ζ to be computed, which provides a scaling law similar to that of Rosner et al. (1978). The relationship between peak temperature and the surface heating rate (i.e., $T_{\max} \propto Q_\odot^{2/7}$) is identical to that of RTV, which conveys that the general nature of this scaling law does not depend on the inclusion or neglect of radiative losses.

The above solution for $y(x)$ exhibits a maximum value at a radial distance that depends inversely on the exponent ψ . A more rapidly dropping heating rate corresponds naturally to a temperature that reaches its peak value closer to the Sun. At large distances from the Sun, the above solution behaves as $y \propto 1/x$, which implies $T \propto r^{-2/7}$ as originally described by Chapman (1957) for a conduction-dominated corona. Our semi-empirical description of the solar wind in Section 4.2 makes use of a slight modification to equation (A4), which is

$$y = \left(\frac{T}{T_{\max}} \right)^{1/\delta}. \quad (\text{A12})$$

This allows the large-scale temperature dropoff to be more freely adjustable as $T \propto r^{-\delta}$. However, it also means that the solution no longer exactly satisfies equations (A1)–(A3). Thus, this δ -modification should be viewed only as a convenient parameterization and not reflective of real physics.

Data Availability Statement

Model data generated for this paper, including some “data behind the figures” and other supplemental information, have been published to the Zenodo data repository and are available in Cranmer (2021). Other observational data used in this paper have all been obtained from previously published sources (see, e.g., Pilipp et al., 1990; Scime et al., 2001; Cranmer et al., 2009; Wilson et al., 2019a; Halekas et al., 2020; Maksimovic et al., 2020; Halekas et al., 2021; Scherer et al., 2021).

Acknowledgments

The authors gratefully acknowledge Jack Scudder for many valuable discussions. The authors are also grateful to the anonymous referee for constructive suggestions that have improved this paper. This work was supported by the National Science Foundation (NSF) Graduate Research Fellowship Program under grant 1650115. Additional support came from the National Aeronautics and Space Administration (NASA), under grants NNX-16AG87G and 80NSSC20K1319, and from the NSF under grant 1613207. This research made extensive use of NASA’s Astrophysics Data System (ADS). The data on which this article is based are available in Cranmer (2021).

References

- Aschwanden, M. J., Schrijver, C. J., & Alexander, D. (2001). Modeling of coronal EUV loops observed with TRACE, I: Hydrostatic solutions with nonuniform heating. *The Astrophysical Journal*, *550*, 1036–1050. <https://doi.org/10.1086/319796>
- Azzalini, A., & Capitanio, A. (2014). *The skew-normal and related families* (IMS Monographs). Cambridge, UK: Cambridge University Press.
- Bale, S. D., Pulupa, M., Salem, C., Chen, C. H. K., & Quataert, E. (2013). Electron heat conduction in the solar wind: Transition from Spitzer-Härm to the collisionless limit. *The Astrophysical Journal Letters*, *769*, L22. <https://doi.org/10.1088/2041-8205/769/2/L22>
- Bame, S. J., McComas, D. J., Barraclough, B. L., Phillips, J. L., Sofaly, K. J., Chavez, J. C., et al. (1992). The Ulysses solar wind plasma experiment. *Astronomy & Astrophysics Supplement Series*, *92*, 237–265. <https://ui.adsabs.harvard.edu/abs/1992A&AS...92..237B/abstract>
- Barakat, A. R., & Schunk, R. W. (1982). Transport equations for multicomponent anisotropic space plasmas: A review. *Plasma Physics*, *24*, 389–418. <https://doi.org/10.1088/0032-1028/24/4/004>
- Bhatnagar, P. L., Gross, E. P., & Krook, M. (1954). A model for collision processes in gases, I: Small amplitude processes in charged and neutral one-component systems. *Physical Review*, *94*, 511–525. <https://doi.org/10.1103/PhysRev.94.511>
- Blelly, P.-L., & Schunk, R. W. (1993). A comparative study of the time-dependent standard 8-, 13- and 16-moment transport formulations of the polar wind. *Annales Geophysicae*, *11*, 443–469. <https://ui.adsabs.harvard.edu/abs/1993AnGeo...11..443B/abstract>
- Bradshaw, S. J., Emslie, A. G., Bian, N. H., & Kontar, E. P. (2019). Coronal loop scaling laws for various forms of parallel heat conduction. *The Astrophysical Journal*, *880*, 80. <https://doi.org/10.3847/1538-4357/ab287f>

- Braginskii, S. I. (1965). Transport processes in a plasma. *Reviews of Plasma Physics*, 1, 205–311. <https://ui.adsabs.harvard.edu/abs/1965RvPP...1..205B/abstract>
- Canullo, M. V., Costa, A., & Ferro-Fontan, C. (1996). Nonlocal heat transport in the solar wind. *The Astrophysical Journal*, 462, 1005–1010. <https://doi.org/10.1086/177214>
- Chapman, S. (1957). Notes on the solar corona and the terrestrial ionosphere. *Smithsonian Contributions to Astrophysics*, 2, 1–12. <https://ui.adsabs.harvard.edu/abs/1957SCoA...2....1C/abstract>
- Chapman, S., & Cowling, T. G. (1970). *The mathematical theory of non-uniform gases*, 3rd ed. Cambridge, UK: Cambridge University Press. <https://ui.adsabs.harvard.edu/abs/1970mtnu.book....C/abstract>
- Che, H., & Goldstein, M. L. (2014). The origin of non-Maxwellian solar wind electron velocity distribution function: Connection to nanoflares in the solar corona. *The Astrophysical Journal Letters*, 795, L38. <https://doi.org/10.1088/2041-8205/795/2/L38>
- Chiuderi, C., Pietrini, P., & Torricelli-Ciamponi, G. (2011). A new fluid scheme for weakly collisional plasmas, I: General theory. *Journal of Geophysical Research*, 116, A04107. <https://doi.org/10.1029/2010JA016395>
- Chust, T., & Belmont, G. (2006). Closure of fluid equations in collisionless magnetoplasmas. *Physics of Plasmas*, 13, 012506. <https://doi.org/10.1063/1.2138568>
- Cowie, L. L., & McKie, C. F. (1977). The evaporation of spherical clouds in a hot gas, I: Classical and saturated mass loss rates. *The Astrophysical Journal*, 211, 135–146. <https://doi.org/10.1086/154911>
- Cranmer, S. R. (2020). Updated measurements of proton, electron, and oxygen temperatures in the fast solar wind. *Research Notes of the AAS*, 4, 249. <https://doi.org/10.3847/2515-5172/abd5ae>
- Cranmer, S. R. (2021). Data files associated with “Electron heat flux in the solar wind: Generalized approaches to fluid transport with a variety of skewed velocity distributions.” Zenodo. <https://doi.org/10.5281/zenodo.4927860>
- Cranmer, S. R., Matthaeus, W. H., Breech, B. A., & Kasper, J. C. (2009). Empirical constraints on proton and electron heating in the fast solar wind. *The Astrophysical Journal*, 702, 1604–1614. <https://doi.org/10.1088/0004-637X/702/2/1604>
- Cranmer, S. R., & van Ballegoijen, A. A. (2012). Proton, electron, and ion heating in the fast solar wind from nonlinear coupling between Alfvénic and fast-mode turbulence. *The Astrophysical Journal*, 754, 92. <https://doi.org/10.1088/0004-637X/754/2/92>
- Cranmer, S. R., van Ballegoijen, A. A., & Edgar, R. J. (2007). Self-consistent coronal heating and solar wind acceleration from anisotropic magnetohydrodynamic turbulence. *The Astrophysical Journal Supplement*, 171, 520–551. <https://doi.org/10.1086/518001>
- Cuperman, S., & Dryer, M. (1985). On heat conduction in multicomponent, non-Maxwellian spherically symmetric solar wind plasmas. *The Astrophysical Journal*, 298, 414–420. <https://doi.org/10.1086/163625>
- Demars, H. G., & Schunk, R. W. (1979). Transport equations for multispecies plasmas based on individual bi-Maxwellian distributions. *Journal of Physics D: Applied Physics*, 12, 1051–1077. <https://doi.org/10.1088/0022-3727/12/7/011>
- Echim, M. M., Lemaire, J., & Lie-Svendsen, Ø. (2011). A review on solar wind modeling: Kinetic and fluid aspects. *Surveys in Geophysics*, 32, 1–70. <https://doi.org/10.1007/s10712-010-9106-y>
- El-Sakka, A. G., Abdellatif, R. A., & Montasser, S. A. (1985). Free molecular flow of rarefied gas over an oscillating plate under aperiodic external force. *As-*

- trophysics and Space Science*, 109, 259–270. <https://doi.org/10.1007/BF00651272>
- Feldman, W. C., Asbridge, J. R., Bame, S. J., Montgomery, M. D., & Gary, S. P. (1975). Solar wind electrons. *Journal of Geophysical Research*, 80, 4181–4196. <https://doi.org/10.1029/JA080i031p04181>
- Forslund, D. W. (1970). Instabilities associated with heat conduction in the solar wind and their consequences. *Journal of Geophysical Research*, 75, 17–28. <https://doi.org/10.1029/JA075i001p00017>
- García-Colín, L. S., Velasco, R. M., & Uribe, F. J. (2008). Beyond the Navier Stokes equations: Burnett hydrodynamics. *Physics Reports*, 465, 149–189. <https://doi.org/10.1016/j.physrep.2008.04.010>
- Gary, S. P., Feldman, W. C., Forslund, D. W., & Montgomery, M. D. (1975). Heat flux instabilities in the solar wind. *Journal of Geophysical Research*, 80, 4197–4203. <https://doi.org/10.1029/JA080i031p04197>
- Goldstein, B. E., Neugebauer, M., Phillips, J. L., Bame, S., Gosling, J. T., McComas, D., et al. (1996). Ulysses plasma parameters: Latitudinal, radial, and temporal variations. *Astronomy & Astrophysics*, 316, 296–303. <https://ui.adsabs.harvard.edu/abs/1996A&A...316..296G/abstract>
- Gombosi, T. I., & Rasmussen, C. E. (1991). Transport of gyration-dominated space plasmas of thermal origin, I: Generalized transport equations. *Journal of Geophysical Research*, 96, 7759–7778. <https://doi.org/10.1029/91JA00012>
- Gombosi, T. I., van der Holst, B., Manchester, W. B., & Sokolov, I. V. (2018). Extended MHD modeling of the steady solar corona and the solar wind. *Living Reviews in Solar Physics*, 15, 4. <https://doi.org/10.1007/s41116-018-0014-4>
- Grad, H. (1949). On the kinetic theory of rarefied gases. *Communications on Pure and Applied Mathematics*, 2, 331–407. <https://doi.org/10.1002/cpa.3160020403>
- Groth, C. P. T., & McDonald, J. G. (2009). Towards physically realizable and hyperbolic moment closures for kinetic theory. *Continuum Mechanics and Thermodynamics*, 21, 467–493. <https://doi.org/10.1007/s00161-009-0125-1>
- Halekas, J. S., Whittlesey, P., Larson, D. E., McGinnis, D., Bale, S. D., Berthomier, M., et al. (2021). Electron heat flux in the near-Sun environment. *Astronomy & Astrophysics*, 650, A15. <https://doi.org/10.1051/0004-6361/202039256>
- Halekas, J. S., Whittlesey, P., Larson, D. E., McGinnis, D., Maksimovic, M., Berthomier, M., et al. (2020). Electrons in the young solar wind: First results from the Parker Solar Probe. *The Astrophysical Journal Supplement*, 246, 22. <https://doi.org/10.3847/1538-4365/ab4cec>
- Hollweg, J. V. (1974). On electron heat conduction in the solar wind. *Journal of Geophysical Research*, 79, 3845–3850. <https://doi.org/10.1029/JA079i025p03845>
- Hollweg, J. V. (1976). Collisionless electron heat conduction in the solar wind. *Journal of Geophysical Research*, 81, 1649–1658. <https://doi.org/10.1029/JA081i010p01649>
- Horaites, K., Boldyrev, S., Wilson, L. B., Viñas, A. F., & Merka, J. (2018). Kinetic theory and fast wind observations of the electron strahl. *Monthly Notices of the Royal Astronomical Society*, 474, 115–127. <https://doi.org/10.1093/mnras/stx2555>
- Hu, Y. Q., Esser, R., & Habbal, S. R. (1997). A fast solar wind model with anisotropic proton temperature. *Journal of Geophysical Research*, 102, 14661–14676. <https://doi.org/10.1029/97JA01040>
- Hunana, P., Tenerani, A., Zank, G. P., Khomeiko, E., Goldstein, M. L., Webb, G. M., et al. (2019a). An introductory guide to fluid models with anisotropic temperatures, part 1: CGL description and collisionless fluid hierarchy. *Journal of Plasma Physics*, 85, 205850602. <https://doi.org/10.1017/>

S0022377819000801

- Hunana, P., Tenerani, A., Zank, G. P., Goldstein, M. L., Webb, G. M., Khomenko, E., et al. (2019b). An introductory guide to fluid models with anisotropic temperatures, part 1: Kinetic theory, Padé approximants, and Landau fluid closures. *Journal of Plasma Physics*, *85*, 205850603. <https://doi.org/10.1017/S0022377819000850>
- Innocenti, M. E., Boella, E., Tenerani, A., & Velli, M. (2020). Collisionless heat flux regulation via the electron firehose instability in the presence of a core and suprathermal population in the expanding solar wind. *The Astrophysical Journal Letters*, *898*, L41. <https://doi.org/10.3847/2041-8213/aba591>
- Killie, M. A., Janse, Å. M., Lie-Svendsen, Ø., & Leer, E. (2004). Improved transport equations for fully ionized gases. *The Astrophysical Journal*, *604*, 842–849. <https://doi.org/10.1086/382023>
- Kuznetsov, V. D., & Dzhililov, N. S. (2009). Sixteen-moment approximation for a collisionless space plasma: Waves and instabilities. *Plasma Physics Reports*, *35*, 962–975. <https://doi.org/10.1134/S1063780X09110063>
- Landi, S., Matteini, L., & Pantellini, F. (2014). Electron heat flux in the solar wind: Are we observing the collisional limit in the 1 AU data? *The Astrophysical Journal Letters*, *790*, L12. <https://doi.org/10.1088/2041-8205/790/1/L12>
- Lazar, M., Pierrard, V., Poedts, S., & Schlickeiser, R. (2012). Modeling space plasma dynamics with anisotropic kappa distributions. In M. P. Leubner, Z. Vörös (Eds.), *Multi-scale dynamical processes in space and astrophysical plasmas, Astrophysics and Space Science Proceedings* (Vol. 33, pp. 97–107). Berlin: Springer-Verlag.
- Leblanc, F., & Hubert, D. (1997). A generalized model for the proton expansion in astrophysical winds, I: The velocity distribution function representation. *The Astrophysical Journal*, *483*, 464–474. <https://doi.org/10.1086/304232>
- Leblanc, F., & Hubert, D. (1998). A generalized model for the proton expansion in astrophysical winds, II: The associated set of transport equations. *The Astrophysical Journal*, *501*, 375–385. <https://doi.org/10.1086/305789>
- Lemaire, J., & Scherer, M. (1973). Kinetic models of the solar and polar winds. *Reviews of Geophysics and Space Physics*, *11*, 427–468. <https://doi.org/10.1029/RG011i002p00427>
- Levermore, C. D. (1996). Moment closure hierarchies for kinetic theories. *Journal of Statistical Physics*, *83*, 1021–1065. <https://doi.org/10.1007/BF02179552>
- Li, X. (1999). Proton temperature anisotropy in the fast solar wind: A 16-moment bi-Maxwellian model. *Journal of Geophysical Research*, *104*, 19773–19786. <https://doi.org/10.1029/1999JA900255>
- Li, B., & Li, X. (2006). Effects of α particles on the angular momentum loss from the Sun. *Astronomy & Astrophysics*, *456*, 359–365. <https://doi.org/10.1051/0004-6361:20054624>
- Lie-Svendsen, Ø., Leer, E., & Hansteen, V. H. (2001). A 16-moment solar wind model: From the chromosphere to 1 AU. *Journal of Geophysical Research*, *106*, 8217–8232. <https://doi.org/10.1029/2000JA000409>
- Lin, R. P., Larson, D. E., Ergun, R. E., McFadden, J. P., Carlson, C. W., Phan, T. D., et al. (1997). Observations of the solar wind, the bow shock and upstream particles with the Wind 3D plasma instrument. *Advances in Space Research*, *20*, 645–654. [https://doi.org/10.1016/S0273-1177\(97\)00452-3](https://doi.org/10.1016/S0273-1177(97)00452-3)
- Linker, J. A., Mikić, Z., Biesecker, D. A., Forsyth, R. J., Gibson, S. E., Lazarus, A. J., et al. (1999). Magnetohydrodynamic modeling of the solar corona during Whole Sun Month. *Journal of Geophysical Research*, *104*, 9809–9830. <https://doi.org/10.1029/1998JA900159>
- Livadiotis, G., & McComas, D. J. (2013). Understanding kappa distributions: A toolbox for space science and astrophysics. *Space Science Reviews*, *175*, 183–214. <https://doi.org/10.1007/s11214-013-9982-9>

- López, R. A., Lazar, M., Shaaban, S. M., Poedts, S., & Moya, P. S. (2020). Alternative high plasma beta regimes of electron heat-flux instabilities in the solar wind. *The Astrophysical Journal Letters*, *900*, L25. <https://doi.org/10.3847/2041-8213/abaf56>
- Luciani, J. F., Mora, P., & Virmont, J. (1983). Nonlocal heat transport due to steep temperature gradients. *Physical Review Letters*, *51*, 1664–1667. <https://doi.org/10.1103/PhysRevLett.51.1664>
- Maksimovic, M., Bale, S. D., Berčič, L., Bonnell, J. W., Case, A. W., Dudok de Wit, T., et al. (2020). Anticorrelation between the bulk speed and the electron temperature in the pristine solar wind: First results from the Parker Solar Probe and comparison with Helios. *The Astrophysical Journal Supplement*, *246*, 62. <https://doi.org/10.3847/1538-4365/ab61fc>
- Marsch, E. (2006). Kinetic physics of the solar corona and solar wind. *Living Reviews in Solar Physics*, *3*, 1. <https://doi.org/10.12942/lrsp-2006-1>
- Martens, P. C. H. (2010). Scaling laws and temperature profiles for solar and stellar coronal loops with non-uniform heating. *The Astrophysical Journal*, *714*, 1290–1304. <https://doi.org/10.1088/0004-637X/714/2/1290>
- Meyer-Vernet, N. (1999). How does the solar wind blow? A simple kinetic model. *European Journal of Physics*, *20*, 167–176. <https://doi.org/10.1088/0143-0807/20/3/006>
- Micera, A., Zhukov, A. N., López, R. A., Innocenti, M. E., Lazar, M., Boella, E., & Lapenta, G. (2020). Particle-in-cell simulation of whistler heat-flux instabilities in the solar wind: Heat-flux regulation and electron halo formation. *The Astrophysical Journal Letters*, *903*, L23. <https://doi.org/10.3847/2041-8213/abc0e8>
- Mintzer, D. (1965). Generalized orthogonal polynomial solutions of the Boltzmann equation. *Physics of Fluids*, *8*, 1076–1090. <https://doi.org/10.1063/1.1761357>
- Morse, R. L., & Nielson, C. W. (1973). Occurrence of high-energy electrons and surface expansion in laser-heated target plasmas. *Physics of Fluids*, *16*, 909–920. <https://doi.org/10.1063/1.1694445>
- Narayan, R., & Medvedev, M. V. (2001). Thermal conduction in clusters of galaxies. *The Astrophysical Journal Letters*, *562*, L129–L132. <https://doi.org/10.1086/338325>
- O’Hagan, A., & Leonard, T. (1976). Bayes estimation subject to uncertainty about parameter constraints. *Biometrika*, *63*, 201–203. <https://doi.org/10.1093/biomet/63.1.201>
- Olbert, S. (1968). Summary of experimental results from MIT detector on IMP-1. In R. L. Carovillano, J. F. McClay, H. R. Radoski (Eds.), *Physics of the Magnetosphere*, Astrophysics and Space Science Library (Vol. 10, pp. 641–659). Dordrecht: Reidel.
- Olsen, E. L., & Leer, E. (1996). Thermally driven one-fluid electron-proton solar wind: Eight-moment approximation. *The Astrophysical Journal*, *462*, 982–996. <https://doi.org/10.1086/177212>
- Olsen, E. L., & Leer, E. (1999). A study of solar wind acceleration based on gyrotopic transport equations. *Journal of Geophysical Research*, *104*, 9963–9974. <https://doi.org/10.1029/1998JA900152>
- Parker, E. N. (1958). Dynamics of the interplanetary gas and magnetic fields. *The Astrophysical Journal*, *128*, 664–676. <https://doi.org/10.1086/146579>
- Parker, E. N. (1964). Dynamical properties of stellar coronas and stellar winds, II: Integration of the heat-flow equation. *The Astrophysical Journal*, *139*, 93–122. <https://doi.org/10.1086/147741>
- Perkins, F. (1973). Heat conductivity, plasma instabilities, and radio star scintillations in the solar wind. *The Astrophysical Journal*, *179*, 637–642. <https://doi.org/10.1086/151902>

- Pilipp, W. G., Miggenrieder, H., Montgomery, M. D., Mühlhäuser, K.-H., Rosenbauer, H., & Schwenn, R. (1987). Characteristics of electron velocity distribution functions in the solar wind derived from the Helios plasma experiment. *Journal of Geophysical Research*, *92*, 1075–1092. <https://doi.org/10.1029/JA092iA02p01075>
- Pilipp, W. G., Miggenrieder, H., Mühlhäuser, K.-H., Rosenbauer, H., & Schwenn, R. (1990). Large-scale variations of thermal electron parameters in the solar wind between 0.3 and 1 AU. *Journal of Geophysical Research*, *95*, 6305–6329. <https://doi.org/10.1029/JA095iA05p06305>
- Rosner, R., Tucker, W. H., & Vaiana, G. S. (1978). Dynamics of the quiescent solar corona. *The Astrophysical Journal*, *220*, 643–665. <https://doi.org/10.1086/155949>
- Salem, C., Hubert, D., Lacombe, C., Bale, S. D., Mangeney, A., Larson, D. E., & Lin, R. P. (2003). Electron properties and Coulomb collisions in the solar wind at 1 AU: Wind observations. *The Astrophysical Journal*, *585*, 1147–1157. <https://doi.org/10.1086/346185>
- Scherer, K., Husidic, E., Lazar, M., & Fichtner, H. (2021). Generalized anisotropic κ -cookbook: 2D fitting of Ulysses electron data. *Monthly Notices of the Royal Astronomical Society*, *501*, 606–613. <https://doi.org/10.1093/mnras/staa3641>
- Schiff, A. J. (2020). Thermal conduction in the solar corona: Origins and applications, (Doctoral dissertation). Retrieved from ProQuest. (<https://search.proquest.com/docview/2407623702/>). Boulder, CO: University of Colorado Boulder.
- Schunk, R. W. (1977). Mathematical structure of transport equations for multispecies flows. *Reviews of Geophysics and Space Physics*, *15*, 429–445. <https://doi.org/10.1029/RG015i004p00429>
- Schwadron, N. A., & McComas, D. J. (2003). Solar wind scaling law. *The Astrophysical Journal*, *599*, 1395–1403. <https://doi.org/10.1086/379541>
- Scime, E. E., Bame, S. J., Feldman, W. C., Gary, S. P., Phillips, J. L., & Balogh, A. (1994). Regulation of the solar wind electron heat flux from 1 to 5 AU: Ulysses observations. *Journal of Geophysical Research*, *99*, 23401–23410. <https://doi.org/10.1029/94JA02068>
- Scime, E. E., Littleton, J. E., Gary, S. P., Skoug, R., & Lin, N. (2001). Solar cycle variations in the electron heat flux: Ulysses observations. *Geophysical Research Letters*, *28*, 2169–2172. <https://doi.org/10.1029/2001GL012925>
- Scudder, J. D. (2019). The long-standing closure crisis in coronal plasmas. *The Astrophysical Journal*, *885*, 148. <https://doi.org/10.3847/1538-4357/ab48e0>
- Scudder, J. D. (2021). Quality metric for Spitzer-Braginskii and Grad 8 moment heat flux closures. *The Astrophysical Journal*, *907*, 90. <https://doi.org/10.3847/1538-4357/abc475>
- Serio, S., Peres, G., Vaiana, G. S., Golub, L., & Rosner, R. (1981). Closed coronal structures, II: Generalized hydrostatic model. *The Astrophysical Journal*, *243*, 288–300. <https://doi.org/10.1086/158597>
- Shaaban, S. M., Lazar, M., & Poedts, S. (2018). Clarifying the solar wind heat flux instabilities. *Monthly Notices of the Royal Astronomical Society*, *480*, 310–319. <https://doi.org/10.1093/mnras/sty1567>
- Smith, D. F., & Lillequist, C. G. (1979). Confinement of hot, hard X-ray producing electrons in solar flares. *The Astrophysical Journal*, *232*, 582–589. <https://doi.org/10.1086/157316>
- Spitzer, L., & Härm, R. (1953). Transport phenomena in a completely ionized gas. *Physical Review*, *89*, 977–981. <https://doi.org/10.1103/PhysRev.89.977>
- Stawarz, J. E., Smith, C. W., Vasquez, B. J., Forman, M. A., & MacBride, B. T. (2009). The turbulent cascade and proton heating in the solar wind at 1 AU. *The Astrophysical Journal*, *697*, 1119–1127. <https://doi.org/10.1088/>

0004-637X/697/2/1119

- Struchtrup, H. (2005). *Macroscopic transport equations for rarefied gas flows: Approximation methods in kinetic theory*. Berlin: Springer-Verlag.
- Struchtrup, H., & Torrilhon, M. (2003). Regularization of Grad's 13 moment equations: Derivation and linear analysis. *Physics of Fluids*, *15*, 2668–2680. <https://doi.org/10.1063/1.1597472>
- Štverák, Š., Maksimovic, M., Trávníček, P. M., Marsch, E., Fazakerley, A. N., & Scime, E. E. (2009). Radial evolution of nonthermal electron populations in the low-latitude solar wind: Helios, Cluster, and Ulysses Observations. *Journal of Geophysical Research*, *114*, A05104. <https://doi.org/10.1029/2008JA013883>
- Štverák, Š., Trávníček, P. M., & Hellinger, P. (2015). Electron energetics in the expanding solar wind via Helios observations. *Journal of Geophysical Research*, *120*, 8177–8193. <https://doi.org/10.1002/2015JA021368>
- Summers, D., & Thorne, R. M. (1992). A new tool for analyzing microinstabilities in space plasmas modeled by a generalized Lorentzian (κ) distribution. *Journal of Geophysical Research*, *97*, 16827–16832. <https://doi.org/10.1029/92JA01664>
- Tong, Y., Vasko, I. Y., Pulupa, M., Mozer, F. S., Bale, S. D., Artemyev, A. V., & Krasnoselskikh, V. (2019). Whistler wave generation by halo electrons in the solar wind. *The Astrophysical Journal Letters*, *870*, L6. <https://doi.org/10.3847/2041-8213/aaf734>
- Vasquez, B. J., Smith, C. W., Hamilton, K., MacBride, B. T., & Leamon, R. J. (2007). Evaluation of the turbulent energy cascade rates from the upper inertial range in the solar wind at 1 AU. *Journal of Geophysical Research*, *112*, A07101. <https://doi.org/10.1029/2007JA012305>
- Vasyliunas, V. M. (1968). A survey of low-energy electrons in the evening sector of the magnetosphere with OGO 1 and OGO 3. *Journal of Geophysical Research*, *73*, 2839–2884. <https://doi.org/10.1029/JA073i009p02839>
- Verscharen, D., Klein, K. G., & Maruca, B. A. (2019). The multi-scale nature of the solar wind. *Living Reviews in Solar Physics*, *16*, 5. <https://doi.org/10.1007/s41116-019-0021-0>
- Viall, N. M., & Borovsky, J. E. (2020). Nine outstanding questions of solar wind physics. *Journal of Geophysical Research*, *125*, e26005. <https://doi.org/10.1029/2018JA026005>
- Voit, G. M. (2011). Quasi-steady configurations of conductive intracluster media. *The Astrophysical Journal*, *740*, 28. <https://doi.org/10.1088/0004-637X/740/1/28>
- Wang, L., Liu, Y., He, J., Tu, C., Pei, Z., Wimmer-Schweingruber, R. F., & Bale, S. D. (2015). Solar wind ~ 20 –200 keV superhalo electrons at quiet times. *The Astrophysical Journal Letters*, *803*, L2. <https://doi.org/10.1088/2041-8205/803/1/L2>
- Wang, Y.-M. (1993). Flux-tube divergence, coronal heating, and the solar wind. *The Astrophysical Journal Letters*, *410*, L123–L126. <https://doi.org/10.1086/186895>
- Whang, Y. C. (1971). Higher moment equations and the distribution function of the solar-wind plasma. *Journal of Geophysical Research*, *76*, 7503–7507. <https://doi.org/10.1029/JA076i031p07503>
- Wheaton, J. H., & Woo, S.-B. (1972). Ion velocity distribution of a weakly ionized gas in a uniform electric field of arbitrary strength. *Physical Review A*, *6*, 2319–2325. <https://doi.org/10.1103/PhysRevA.6.2319>
- Wilson, L. B., III, Chen, L.-J., Wang, S., Schwartz, S. J., Turner, D. L., Stevens, M. L., et al. (2019a). Electron energy partition across interplanetary shocks, I: Methodology and data product. *The Astrophysical Journal Supplement*, *243*, 8. <https://doi.org/10.3847/1538-4365/ab22bd>

- Wilson, L. B., III, Chen, L.-J., Wang, S., Schwartz, S. J., Turner, D. L., Stevens, M. L., et al. (2019b). Electron energy partition across interplanetary shocks, II: Statistics. *The Astrophysical Journal Supplement*, *245*, 24. <https://doi.org/10.3847/1538-4365/ab5445>
- Wilson, L. B., III, Chen, L.-J., Wang, S., Schwartz, S. J., Turner, D. L., Stevens, M. L., et al. (2020). Electron energy partition across interplanetary shocks, III: Analysis. *The Astrophysical Journal*, *893*, 22. <https://doi.org/10.3847/1538-4357/ab7d39>
- Withbroe, G. L. (1988). The temperature structure, mass, and energy flow in the corona and inner solar wind. *The Astrophysical Journal*, *325*, 442–467. <https://doi.org/10.1086/166015>
- Wu, J., & Taieb, C. (1993). Heat flux solutions of the 13-moment approximation transport equations in a multispecies gas. *Journal of Geophysical Research*, *98*, 15613–15620. <https://doi.org/10.1029/93JA00643>
- Yamaguchi, Y. Y. (2015). Nondiagonalizable and nondivergent susceptibility tensor in the Hamiltonian mean-field model with asymmetric momentum distributions. *Physical Review E*, *92*, 032109. <https://doi.org/10.1103/PhysRevE.92.032109>
- Zawaideh, E., Kim, N. S., & Najmabadi, F. (1988). Generalized parallel heat transport equations in collisional to weakly collisional plasmas. *Physics of Fluids*, *31*, 3280–3285. <https://doi.org/10.1063/1.866940>
- Zouganelis, I., Maksimovic, M., Meyer-Vernet, N., Lamy, H., & Issautier, K. (2004). A transonic collisionless model of the solar wind. *The Astrophysical Journal*, *606*, 542–554. <https://doi.org/10.1086/382866>